

148115
P.36

REPORT TO THE
NATIONAL AERONAUTICS AND SPACE ADMINISTRATION

SEMIANNUAL STATUS REPORT #4

for
GRANT NAG 5-1490

INVESTIGATION OF PASSIVE ATMOSPHERIC SOUNDING
USING
MILLIMETER AND SUBMILLIMETER WAVELENGTH CHANNELS

A.J. Gasiewski (Principal Investigator)

L.K. Adelberg (Graduate Student)
D.B. Kunkee (Graduate Student)
D.M. Jackson (Graduate Student)

Covering the period from
July 1, 1992 to December 31, 1992

Submitted by:

Professor Albin J. Gasiewski
School of Electrical Engineering
Georgia Institute of Technology
Atlanta, Georgia, 30332-0250
(404) 894-2934

NASA Technical Officer:

Dr. Robert F. Adler
Laboratory for Atmospheres/Code 612
NASA Goddard Space Flight Center
Greenbelt, MD 20771
(301) 286-9086

(NASA-CR-192305) INVESTIGATION OF
PASSIVE ATMOSPHERIC SOUNDING USING
MILLIMETER AND SUBMILLIMETER
WAVELENGTH CHANNELS Semiannual
Status Report No. 4, 1 Jul. - 31
Dec. 1992 (Georgia Inst. of Tech.)
36 p
N93-19036
Unclass
G3/46 0148115

TABLE OF CONTENTS

I.	INTRODUCTION	1
II.	SUMMARY OF ACTIVITIES	3
III.	CONCLUSIONS AND PLANS FOR FUTURE WORK	7
IV.	REFERENCES	11
V.	TABLES AND FIGURES	13
V.	APPENDIX A	17
VI.	APPENDIX B	29
VII.	APPENDIX C	30
VI.	APPENDIX D	34

INTRODUCTION

Progress by investigators at the Georgia Institute of Technology in the development of techniques for passive microwave retrieval of water vapor, cloud and precipitation parameters using millimeter- and sub-millimeter wavelength channels is reviewed. Channels of particular interest are in the tropospheric transmission windows at 90, 166, 220, 340 and 410 GHz and centered around the water vapor lines at 183 and 325 GHz. Collectively, these channels have potential application in high-resolution mapping (e.g., from geosynchronous orbit), remote sensing of cloud and precipitation parameters, and retrieval of water vapor profiles.

During the period from July 1, 1992 through December 31, 1992, the Millimeter-wave Imaging Radiometer (MIR) completed successful clear-air data flights on the NASA ER-2. Coincident data was collected from several other sources, including the DMSP SSM/T-2 satellite, collocated radiosondes, a ground-based Raman lidar, the Millimeter-wave Temperature Sounder (MTS) and infrared imagers.

Optimal calibration of the MIR using a Wiener filter to facilitate estimating the instrument's gain and offset has been demonstrated. Preliminary reduction of the clear-air flight data shows good agreement between MIR and SSM/T-2 brightnesses, although some unexplained random discrepancies have been found between zenith MIR brightnesses at 89, 150, and 220 GHz and radiosonde-based calculations.

In order to resolve questions concerning the absolute calibration of both the MIR and similar microwave sounders, the investigation of the scattering and emission from microwave blackbody calibration loads has continued. A new analytical formulation of the coupled wave method for lossy period surfaces has been developed, and an extension of the method to two-dimensional periodic structures is being developed. A preliminary thermal analysis for the wedge-type load has also been developed.

Integration of three submillimeter-wave channels on the MIR at 325 \pm 1, 3, and 8 GHz is proceeding, and should be completed in time to allow data flights during the Tropical Ocean Global Atmosphere/Coupled Ocean-Atmosphere Response Experiment (TOGA/COARE, January-February 1993).

A new study commenced under this grant is the investigation of the utility of the third Stokes parameter $T_U = \langle E_V E_H^* \rangle$ for passive remote sensing of both ocean wave direction and oriented ice particles in cirrus clouds. To this end, a cross-correlation channel has been installed on the 92-GHz fixed-beam slant-path radiometer to be flown on the NASA DC-8 during TOGA/COARE. An external polarized calibration load for use during TOGA/COARE has also been developed.

SUMMARY OF ACTIVITIES

Activities within the period from July 1, 1992 through December 31, 1992 by Georgia Tech researchers in millimeter and submillimeter wavelength tropospheric remote sensing have been centered around the calibration of the Millimeter-wave Imaging Radiometer (MIR), preliminary flight data analysis, and preparation for TOGA/COARE. The MIR instrument is a joint project between NASA/GSFC and Georgia Tech. In the current configuration, the MIR has channels at 90, 150, 183+/-1,3,7, and 220 GHz. Provisions for three additional channels at 325+/-1,3 and 8 GHz have been made, and a 325-GHz receiver is currently being built by the ZAX Millimeter Wave Corporation for use in the MIR. Past Georgia Tech contributions to the MIR and its related scientific uses have included basic system design studies, performance analyses, and circuit and radiometric load design, in-flight software, and post-flight data display software.

The combination of the above millimeter wave and submillimeter wave channels aboard a single well-calibrated instrument will provide unique radiometric data for radiative transfer and cloud and water vapor retrieval studies. A paper by the PI discussing the potential benefits of passive millimeter- and submillimeter wave observations for cloud, water vapor and precipitation measurements has recently been published ([Gasiewski, 1992], see Appendix A).

1. MIR Data Analysis

At this time, all MIR hardware and software (both in-flight and post-flight) for unattended operation aboard the NASA ER-2 has been completed. The robustness of the instrument has been demonstrated by three data flights during May, 1992 (13 flight hours) and six data flights (27 flight hours) during June-July, 1992. A summary of the 1992 MIR flights to date is shown in Table 1. Applicable data from other instruments, including the Massachusetts Institute of Technology's Millimeter-wave Temperature Sounder (MIS), the NASA Airborne Ocean Color Imager (AOCI), the DMSP SSM/T-2 radiometric sounder, the NASA/GSFC Raman water vapor lidar, and collocated radiosondes is available and currently being compiled.

MIR calibration is accomplished using hot and cold blackbody load views (once per scan) along with appropriately weighted temperature values from eight resistive temperature sensors located on the loads. Previously, a causal infinite impulse response (IIR) discrete filter was used to provide quick estimates of the instrument gain and offset values from the noisy single-scan estimates. Recently, software has been written to demonstrate the application of an optimal non-causal filter (the Wiener filter) to estimate MIR gains and offsets ([Adelberg et al, 1993], see Appendix B). The filter coefficients are derived from estimates of the autocorrelation functions for the gain and offsets of the instrument. A comparison of the estimated gains for the 89-GHz channel using the IIR (Fig. 1b) and Wiener filter (Fig. 1c) illustrates that a significant reduction in calibration noise is obtained using the optimal filter.

The optimal calibration software also includes a nonlinear jump detector based on a statistical Z-test to identify stable periods of operation. Within these periods the linear Wiener filter is applied. The calibration software is currently being incorporated into a user-friendly package for distribution to MIR investigators at GSFC and Georgia Tech.

An analysis of clear-air data observed using the MIR during the June-July deployment suggests generally good agreement with coincident down-looking brightnesses observed by the SSM/T-2 satellite [Wang et al, 1993]. Further comparisons using up-looking observations and radiative transfer calculations based on coincident radiosonde measurements show apparently random differences of up to ± 40 K in the 89, 150, and 220 GHz channels (Fig. 2). These differences are hypothesized to be caused by either MIR calibration or radiosonde error in water vapor measurements at altitudes above ~ 5 km. A more comprehensive analysis using a larger set of coincident soundings is underway.

2. Calibration Load Analysis

In a recent publication by Gasiewski and Jackson [1992], the coupled wave method [Moharam and Gaylord, 1982] for determining the reflectivity of lossy wedge-type absorbers was verified against measured laboratory data. Since this time, a new formulation of the coupled wave method based upon multiport linear network theory has been developed, and reflectivity

calculations for several wedge absorber geometries have been performed. The TM reflectivity for typical iron-epoxy wedge-type loads with various electrical depths and periods (Fig. 3) provides a basis for the design of wideband radiometric calibration targets.

In order to predict the amount of thermal emission from a calibration target, the temperature distribution over the structure needs to be known. This is particularly critical near the tips of the absorber, where much of the emission occurs and thermal gradients are large. To this end, a steady state thermal analysis of a wedge-type structure has been initiated. The solution to the heat equation is performed using the coupled harmonic method. Preliminary results suggest that thermal gradients near the absorbing (and, hence, emitting) tips of the wedges are significant enough to warrant consideration in calibration load analysis.

3. 325-GHz Receiver for use on the MIR

The implementation of a 325-GHz receiver on the MIR has been a high Georgia Tech priority. A double-balanced Schottky diode mixer employing a subharmonically-pumped local oscillator frequency-doubled Gunn diode source has been fabricated by the ZAX Millimeter-Wave Corporation of San Dimas, CA, and is currently being flight qualified. The double-sideband noise figure attained for the receiver is ~12 dB (4300 K noise temperature), which is acceptable for ascertaining science results at SMMW frequencies. The receiver is expected to be available for integration into the MIR near the end of 1992, and operative on the ER-2 for data flights during TOGA/COARE, January-February, 1993.

4. Polarimetric Microwave Radiometry

While the utility of vertically and horizontally polarized brightness temperatures for both surface and atmospheric remote sensing has long been recognized, the potential use of the third Stokes parameter $T_U = \langle E_v E_h^* \rangle$ in Earth remote sensing has largely been overlooked. However, our recent laboratory measurements using a fresh-water wave tank [Kunkee and Gasiewski, 1993] illustrate a significant dependence of T_U on the propagation direction of the water wave (Fig. 4). The T_U experimental data for the case of a 65° observation angle is well corroborated using a

geometrical optics model for surface reflectivity, although not all incident angles and polarizations agree quite as well. The relatively large amplitude of the T_U signal (± 10 K), along with the observation that T_U is in phase-quadrature with the signals measured in T_V and T_H suggest that remote sensing of ocean wave direction might be facilitated using a spaceborne polarimetric radiometer. Indeed, this has been suggested by Wentz [1992] and Dzura et al [1992].

In addition to striated water surfaces, it is hypothesized that polarimetric microwave signatures in T_V , T_H , and T_U will be produced by oriented ice particles, for example, in electrified cirrus anvils. Indeed, microwave depolarization signatures in space-to-ground communications links have been associated with lightning discharges [Cox and Arnold, 1979].

To test these hypotheses we have performed the necessary electronic and hardware modifications to operate the NASA/GSFC 92-GHz polarimetric radiometer on the NASA DC-8 aircraft during TOGA/COARE. The radiometer, developed under a previous NASA grant (NAG 8-829), permits precise measurement of the first three Stokes' parameters. This is accomplished using a conventional dual-polarization radiometer augmented with a third cross-correlation channel. Accurate calibration is performed using a polarized calibration load [Gasiewski and Kunkee, 1993]. Integration and testing of the polarimetric radiometer was performed at NASA/ARC during December, 1992.¹

In addition to the aircraft integration, additional laboratory measurements of the upwelling polarimetric emission at 92-GHz from moist striated sand and soil were measured. Although signatures in all of the first three Stokes' parameters were measured, a complete analysis of this data is pending.

¹ This is believed to be the first fully polarimetric radiometer to be operated in Earth remote sensing experiments on a US research aircraft. A predecessor 37-GHz instrument was flown during experiments conducted by the Soviets during the late 1980's [Dzura et al, 1992].

CONCLUSIONS AND PLANS FOR FUTURE WORK

To date, Georgia Tech has provided assistance to NASA/GSFC in the mechanical and electrical design of the MIR, and has been primarily responsible for MIR flight and analysis software. At this time, our primary interests are airborne data collection using the MIR, the integration of the 325-GHz receiver into the MIR, and the development of EHF and SMMW meteorological retrieval algorithms.

To assist in the collection of airborne data during TOGA/COARE, at least one Georgia Tech investigator will be present at the COARE aircraft operations site in Townsville, Australia during January-February, 1993. A high priority is assigned to integrating the 325-GHz receiver into the MIR for data flights during TOGA/COARE. At this time, it appears likely that the 325-GHz channels will be operational for at least part of COARE.

The MIR data from TOGA/COARE and the 1992 data flights is currently stored in raw format on high-density 8-mm tapes. For purposes of meteorological data analysis, calibration software incorporating nonlinear Wiener filtering and aircraft roll compensation is being implemented. This will greatly facilitate the clear-air comparisons and cloud and precipitation studies, and will provide a practical means of disseminating optimally calibrated data to collaborating investigators.

Concurrent with the MIR operation, retrievals of water vapor and cloud water content from EHF and SMMW observations will be pursued. One promising method is the non-linear statistical iterative method used by Kuo [1988]. An extension of this technique to include cloud water content, base altitude, cloud thickness and surface emissivity as variable parameters is currently being studied. Another promising method is based on a multidimensional nonlinear map implemented using an artificial neural net. Here, the use of the backpropagation algorithm to train a net consisting of two-layers (of about 10 neurons each) on simulated radiometric data is currently being studied.

To provide sufficient computational capabilities (disk storage capacity and processing speed) to perform the MIR data processing and retrieval studies, we are planning to purchase a Hewlett-Packard model 710

workstation or equivalent 80486-based machine under this grant.

In order to better characterize the RF response and absolute accuracy of the MIR, it is planned to ship the instrument to Georgia Tech for tests, including: (1) RF passband response measurements using a plasma discharge noise source and spectrum analyzer, (2) local oscillator interference and reflection measurements using a movable reflecting plate, and (3) calibration-load foam reflection and transmission measurements. These simple measurements will provide answers to questions concerning the calibration of the MIR and the use of the 183 and 325-GHz data in radiative transfer intercomparisons.

Accurate absolute calibration of the MIR requires that the total reflectivity of the hot and cold loads be less than 1%, and known to better than 0.1%. Manufacturer's specifications typically provide only the specular component of the reflectivity, which is thought to be substantially less than the total reflectivity. In order to refine the MIR calibration, we plan to extend the study of the electromagnetic characteristics of wedge-type blackbody loads to the more desirable pyramidal loads.

Our approach is to develop numerical models for one- and two-dimensionally periodic lossy gratings using the coupled wave method. We currently have software based on the coupled wave method to predict the reflectivity of one-dimensionally periodic loads of arbitrary dielectric profile. Extension of the coupled wave model to two-dimensionally periodic surfaces appears feasible, and will be attempted. In addition to the electromagnetic analysis, work on the steady state thermal analysis for one- and two-dimensionally periodic calibration loads will be continued. Although, the radiometric calibration load reflectivity analysis is of importance in understanding precision radiometer calibration, it is of tertiary importance relative to the EHF and SMMW data collection and analysis.

To further investigate the potential of polarimetric radiometry in remote sensing of surface and atmospheric parameters, the following projects are planned: (1) Airborne fully-polarimetric radiometer observations using the NASA/GSFC 92-GHz radiometer on the NASA DC-8 will be conducted during TOGA/COARE. Of particular interest will be correlations of

between polarimetric signatures in the microwave data and both thunderstorm electrification and ocean wave direction. (2) Continued reduction of laboratory polarimetric radiometer data measured over water waves and both wet and dry sand and soil. Information on the polarizing properties of such surfaces will be useful in remote sensing of ocean characteristics and vegetation as well as understanding the effects of surface emission on passive atmospheric sounding. (3) To reduce the complexity of calibrating a polarimetric radiometer, the design of a digital cross-correlator will be continued. The cross correlator will be a precursor to the one proposed to be used on the NASA/MSFC Advanced Microwave Precipitation Radiometer (AMPR) [Gasiowski and Kunkee, 1992b]. The bandwidth of the cross-correlator will be approximately 500 MHz, making the device useful for wideband radiometric channels.

Recommended Improvements to the MIR

Although the performance of the MIR during airborne and ground-based measurements in 1992 was good, some modifications to improve stability and calibration accuracy are recommended. These include:

1. To minimize calibration uncertainty due to load reflectivity and spillover, it is recommended that both loads be moved closer to the scanning mirror (approximately 2 cm is available), the scan cavity be lined with moderately absorptive material (e.g. "Echosorb") and its approximate temperature monitored, and the antenna beams (behind the lens array) be isolated from each other using thin (2-mm) walls of absorbing material. Some metal brackets should also be shaved in order to provide all 5 MIR feedhorns with unobstructed views of their respective lenses.

2. Precise in-situ sensitivity patterns for all receivers should be measured, including both near and far-zone sensitivities. This will allow the determination of the amount and significance of beam spillover at the calibration loads, as well as provide a check on the beam alignment and focussing. If needed, new calibration load shrouds might be machined to subtend a slightly larger solid angle.

3. A grooved TFX insulator should be designed and fabricated to cover the calibration loads. Using the coupled-wave software, the transparency of the insulator could be optimized for the suite of MIR frequencies. It is expected that such a cover will exhibit less scattering and absorption than

the styrofoam covers currently used, yet provide adequate thermal insulation. Provisions for purging the space behind the load cover with dry nitrogen before flights should be installed.

4. During flights, some instability in the temperatures of the calibration loads and mixer temperatures was noted. For this reason alone, the temperature regulators should be redesigned the nonlinear dynamic thermal responses of the various thermo-electrical circuits considered. However, the current regulators are also quite inefficient in that they are resistive (lossy) in design. Hence, they heat the MIR frame immediately surrounding them considerably. Modified regulators based on lossless switching designs should be used here. Provided proper grounding and shielding practices are followed, interference caused by switching noise from these devices should not occur.

REFERENCES

Adelberg, L.K., A.J. Gasiewski and D.M. Jackson, "Optimal Calibration of Radiometers using Discrete Wiener Filters", submitted for presentation at the 1993 International Geoscience and Remote Sensing Symposium, Tokyo, Japan, August 18-23, 1993.

Cox, D.C., and H.W. Arnold, "Observations of Rapid Changes in the Orientation and Degree of Alignment of Ice Particles Along an Earth-Space Radio Propagation Path", J. Geophys. Res., vol. 84, pp. 5003-5010, 1979.

Dzura, M.S., V.S. Etkin, A.S. Khrupin, M.N. Pospelov, M.D. Raev, "Radiometers-Polarimeters: Principles of Design and Applications for Sea Surface Microwave Emission Polarimetry", Proceedings of the 1992 IEEE International Geoscience and Remote Sensing Symposium (IGARSS), pp. 1432-1434, June, 1992.

Gasiewski, A.J., "Numerical Sensitivity Analysis of Passive EHF and SMMW Channels to Tropospheric Water Vapor, Clouds, and Precipitation", IEEE Trans. Geosci. Remote Sensing, Vol. 30, No. 5, pp. 859-870, September, 1992.

Gasiewski, A.J., D.M. Jackson, and A.F. Peterson, "Electromagnetic Scattering from Lossy Corrugated Surfaces: Application to Microwave Absorbers", Proceedings of the 1991 North American Radio Science Meeting and International IEEE/AP-S Symposium, p 304, University of Western Ontario, June 24-28, 1991.

Gasiewski, A.J., and D.M. Jackson, "Electromagnetic Scattering from Microwave Absorbers: Laboratory Verification of the Coupled Wave Theory", Proceedings of the 1992 IEEE Joint Symposia APS/URSI/EMP Meeting, Chicago, Illinois, July 18-25, 1992.

Gasiewski, A.J., and D.B. Kunkee, "Calibration and Applications of Polarization Correlation Radiometers", To appear in IEEE Trans. Microwave Theory Tech., May, 1993.

Kunkee, D.B., and A.J. Gasiewski, "Laboratory Measurements of Water Gravity Wave Characteristics using Full Polarization Microwave Radiometry", Proceedings of the 1993 URSI National Radio Science Meeting, p 155, presented at the University of Colorado, Boulder, CO, Jan 5-8, 1993.

Wang, J.R., A.J. Gasiewski and V. Falcione, "Microwave Radiometric Water Vapor Profiling: Comparisons of SSM/T-2 and MIR Data", Submitted for presentation at the 1993 Progress in

Electromagnetics Research Symposium (PIERS), Jet Propulsion Laboratory, July 12-16, 1993.

Gasiewski, A.J., and D.B. Kunke, "Airborne Full Polarization Radiometry Using the MSFC Advanced Microwave Precipitation Radiometer (AMPR)", NASA Marshall Space Flight Center Earth Science and Applications Programs 1992 Research Review, Huntsville, AL, July 7-9, 1992b.

Kuo, C.C., "Statistical Iterative Scheme for Estimating Relative Humidity Profiles from Microwave Radiometric Measurements", S.M. Thesis, Massachusetts Institute of Technology, Cambridge, MA, 1988.

Moharam, M.G., and T.K. Gaylord, "Diffraction Analysis of Dielectric Surface Relief Gratings", J. Opt. Soc. Am., 72, 10, 1385-1392, 1982.

Thompson, A.R., J.M. Moran, and G.W. Swenson, Jr., Interferometry and Synthesis in Radio Astronomy, Krieger Publishing Co., Malabar FL, 1991.

Wentz, F.J., "Measurement of Oceanic Wind Vector Using Satellite Microwave Radiometers", IEEE Trans. Geosci. Remote Sensing, vol. 30, no. 5, pp. 960-972, September 1992.

Table 1.

MIR integration and data flights: 1992.

Sortie #	Date	Time (UTC) (JPE)	Instruments & Remarks
92-087	5/11/92	1900-2200	MIR, MTS(u), AOCI
92-089	5/14/92	2315-0515	MIR, MTS(d), AOCI *
92-090	5/15/92	2320-0500	MIR, MTS(u), AOCI *
92-130	7/23/92	2102-2312	MTS(d)
92-131	7/29/92	0659-1325	MTS(d) ++
92-132	7/30/92	0708-1335	MTS(d) ++
92-134	8/2/92	0631-0930	MTS +
92-135	8/3/92	0300-0606	MTS +
92-140	8/6/92	0658-1314	MTS ++

* SSM/T-2 satellite underpass.

+ Ground-based Raman H₂O_v lidar overflight.

Note: "u" or "d" indicate up-looking or down-looking, respectively.

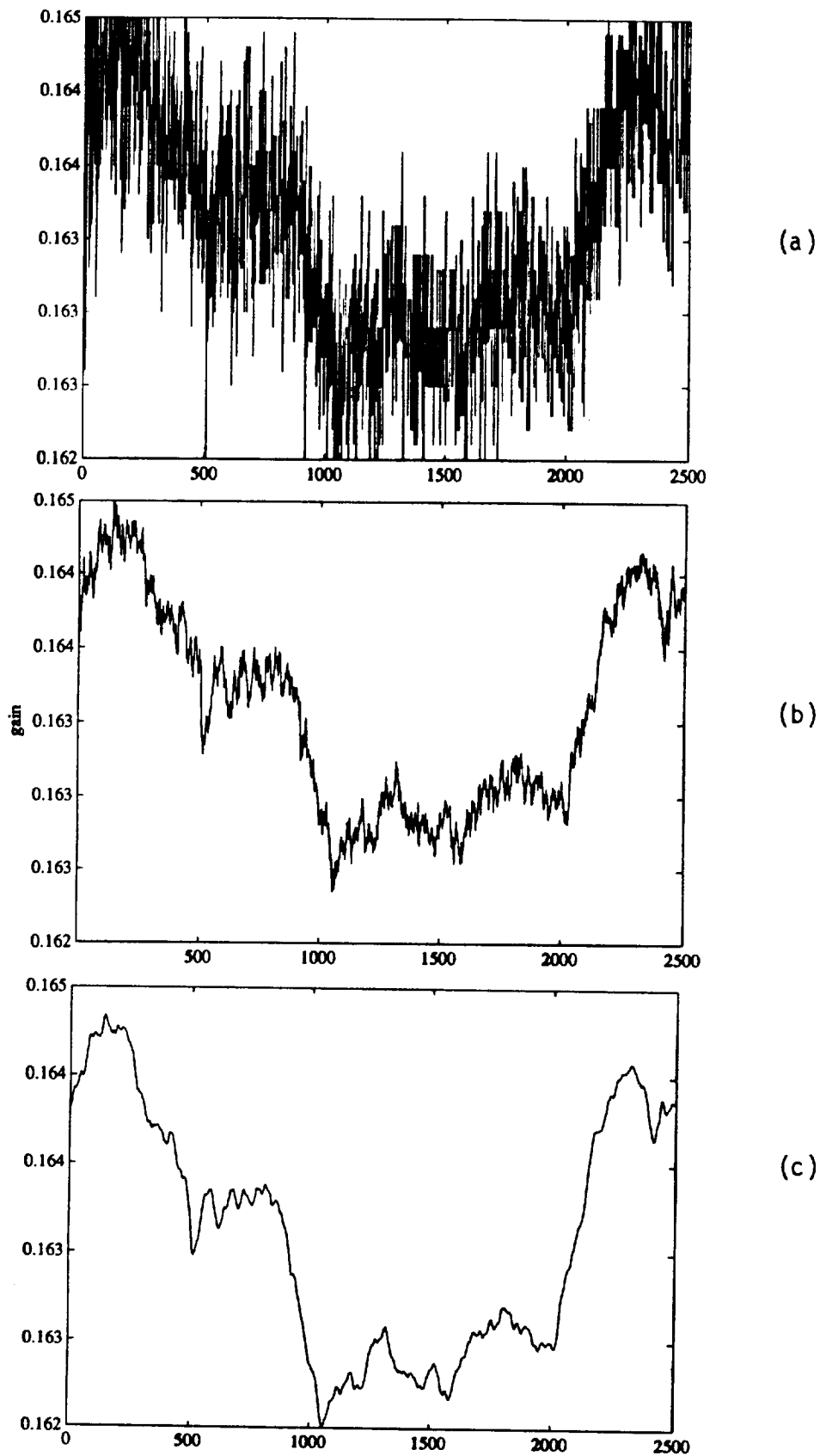


Figure 1: MIR 89-GHz channel gain estimates: (a) single-scan estimates, (b) IIR filtered estimates, using 10% of the current single-spot gain and 90% of the previous estimate, and (c) Wiener filtered estimates.

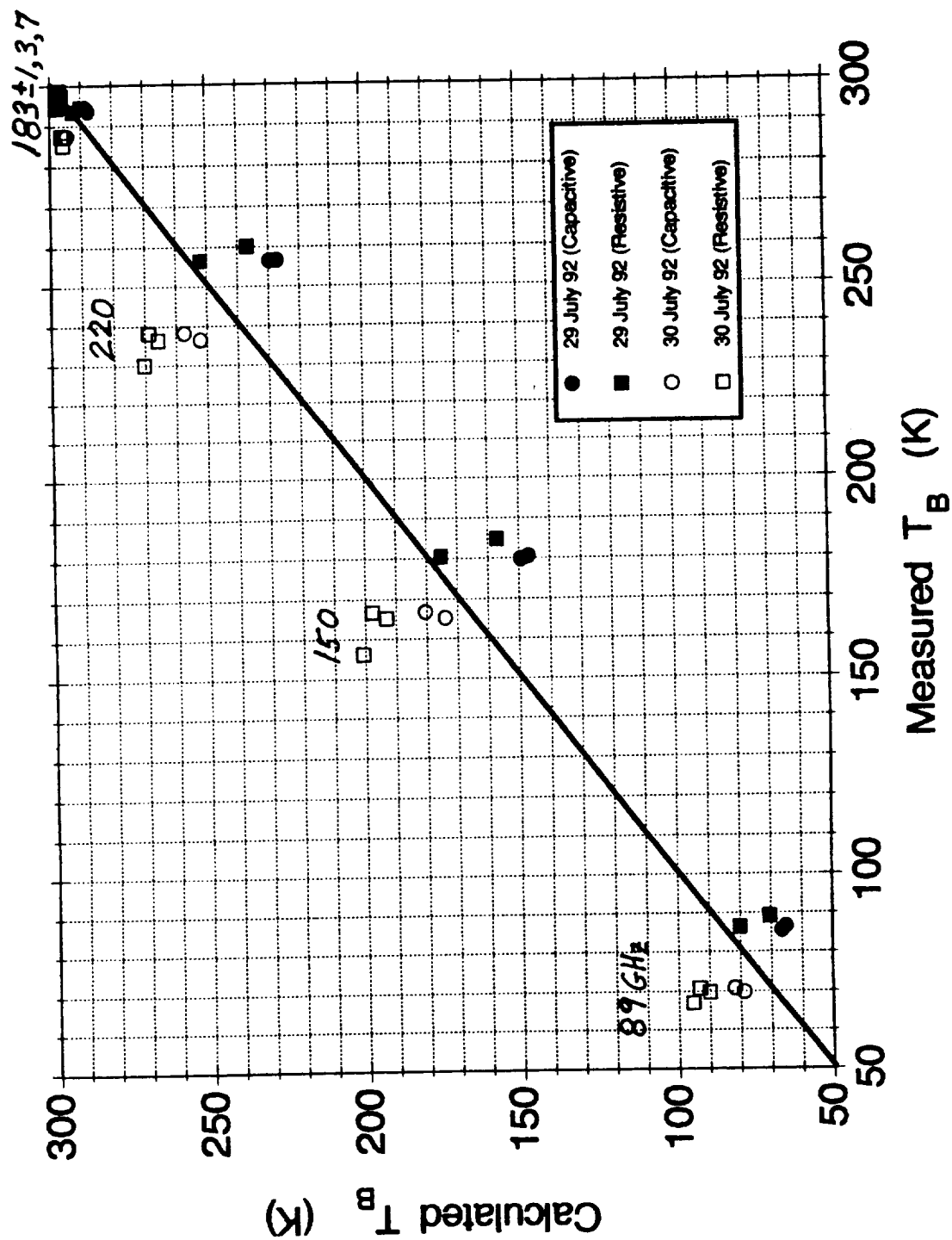


Figure 2. Comparison of observed zenith antenna temperatures with radiosonde-based calculations for the MIR channels. The type of humidity probe (Vaisalla capacitive type or Viz resistive type) is indicated.

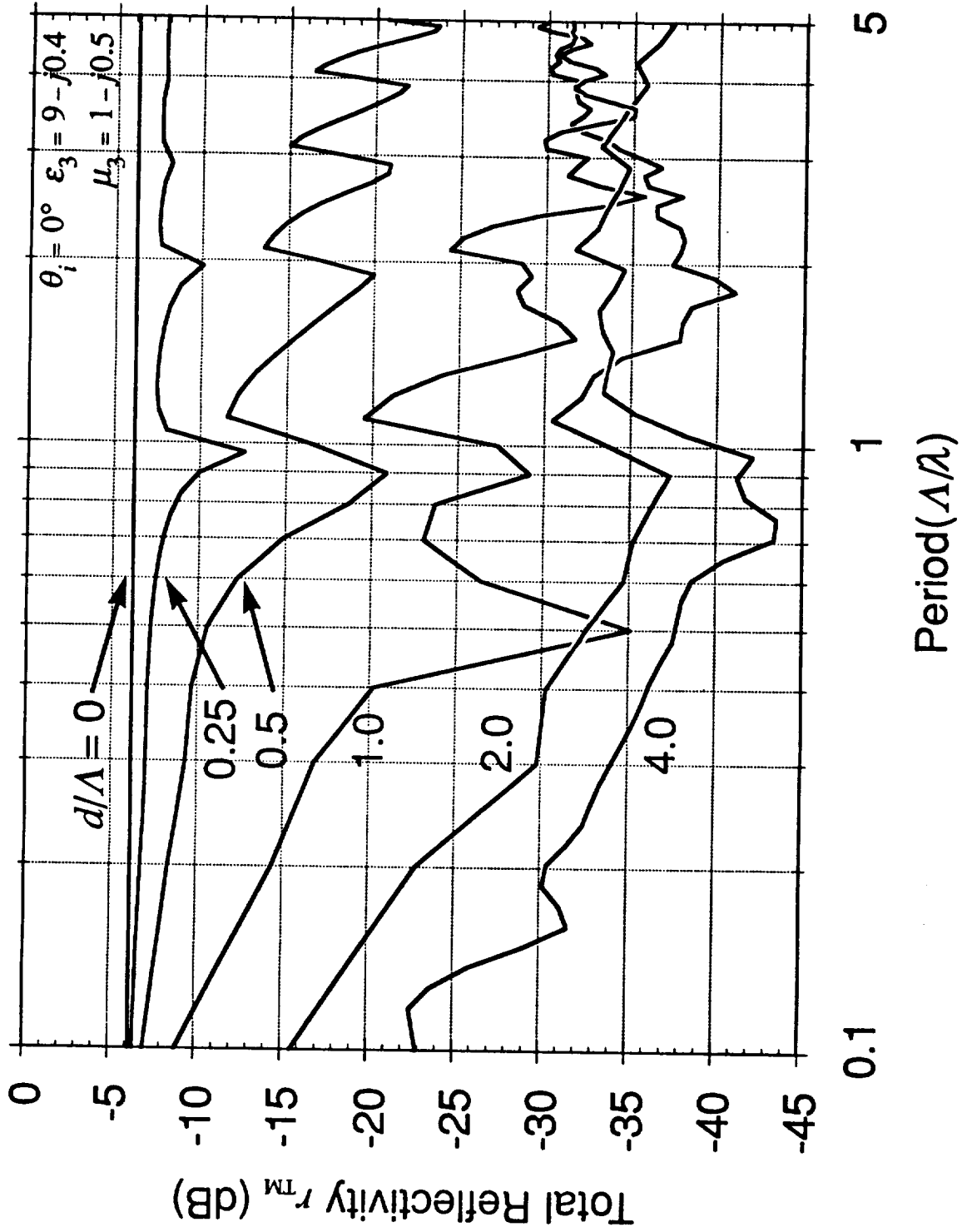


Figure 3: Normal TM reflectivity for wedge-type iron epoxy calibration targets computed using the coupled wave method. The complex permittivity and permeability are $9-j0.4$ and $1-j0.5$, respectively.

Numerical Sensitivity Analysis of Passive EHF and SMMW Channels to Tropospheric Water Vapor, Clouds, and Precipitation

A. J. Gasiewski, *Member, IEEE*

Abstract—Potential uses of specific Extremely High Frequency (EHF) and Sub-Millimeter-Wave (SMMW) channels at 90, 166, 183, 220, 325, 340, and 410 GHz for passive spaceborne remote sensing of the troposphere and lower stratosphere are investigated using an iterative numerical radiative transfer model. Collectively, these channels offer potential for high spatial resolution imaging using diffraction-limited apertures of practical size, along with the ability to profile water vapor, map precipitation beneath optically opaque cloud cover, and to measure nonprecipitating cloud (e.g., cirrus) parameters. The numerical study, along with the results of previous passive microwave experiments, suggests that a widely-spaced set of EHF and SMMW channels can yield observable degrees of freedom related to clouds and precipitation not available by exclusively using the more thoroughly studied microwave channels below 183 GHz. A new passive airborne imaging instrument for tropospheric meteorological sensing at 90, 150, 183 ± 1 , 3, 7, 220, and 325 ± 1 , 3, 9 GHz, the Millimeter-wave Imaging Radiometer (MIR), is described.

I. INTRODUCTION

Spaceborne passive microwave measurements of tropospheric meteorological parameters are impeded by at least two problems: (1) spatial undersampling of the brightness field due to the inherently broad antenna patterns of practical satellite-based microwave imagers, and (2) the adverse effects of heavy, nonprecipitating clouds on both temperature and water vapor retrievals. On occasion, it is also desirable to have enhanced sensitivity to thin clouds (e.g., cirrus) for the purposes of detection and water content estimation. This need contrasts with the primary advantage of microwave observations in relation to infrared (IR) and visible observations, namely, an enhanced ability to probe through most cloud cover.

These problems can be partially alleviated by observing at specific Extremely High Frequency (EHF: 30–300 GHz) and Sub-Millimeter Wave (SMMW: 300+ GHz) passive microwave frequencies. Of particular interest are the EHF and SMMW channels at 220, 325, 340, and 410 GHz, used in conjunction with the more thoroughly investigated (or,

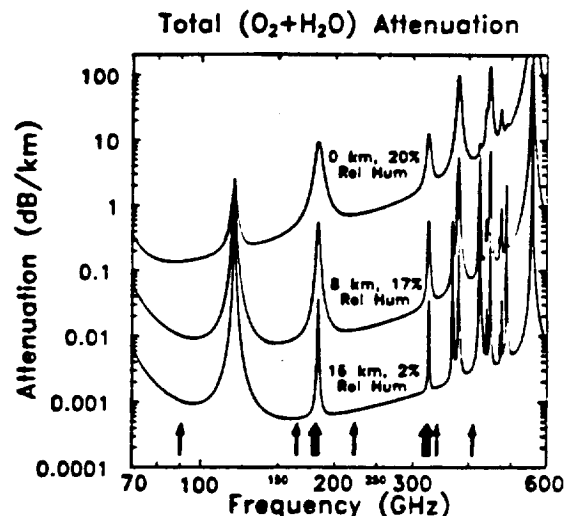


Fig. 1. Tropospheric clear-air EHF and SMMW absorption for several relative humidities. Specific frequencies of interest are indicated by arrows.

“conventional”) microwave channels at 6, 10, 18, 37, 50–60, 90, 118, 166, and 183 GHz. Collectively, these channels sample nearly all significant clear-air tropospheric spectral features (i.e., all O_2 and H_2O absorption lines and transmission windows, see Fig. 1). In particular, they sample the relatively featureless hydrometeor absorption and scattering spectrum over nearly two decades in frequency, spanning the transition from the Rayleigh to the Mie regions for a wide range of precipitation rates (Figs. 2(a) and (b)). Interest in EHF and SMMW channels stems from both (1) the increased spatial resolution available using diffraction-limited apertures of fixed size, and (2) hypothesized observable degrees of freedom related to water vapor, clouds, and precipitation parameters using these channels both alone and coincident with other lower-frequency microwave channels.

This paper discusses the results of a numerical investigation into the tropospheric meteorological observables that can be expected using 220, 325, 340, and 410 GHz satellite-based brightness measurements, both alone and in coincidence with the conventional microwave channels. For purposes of passive sensing, tropospheric absorption is negligible below 6 GHz and generally excessive above 450 GHz. Thus, channels outside this range are not considered. The following potential capabilities of the collective set of channels are addressed:

1. Imaging with enhanced spatial resolution,

Manuscript received July 17, 1991; revised April 17, 1992. This work was supported by the Georgia Institute of Technology and NASA Grants NAG 5-1332 and NAG 5-1490.

The MIR instrument is a joint effort between NASA GSFC and the School of Electrical Engineering at the Georgia Institute of Technology.

The author is with the School of Electrical Engineering, Georgia Institute of Technology, Atlanta, GA 30332-0250.

IEEE Log Number 9202014.

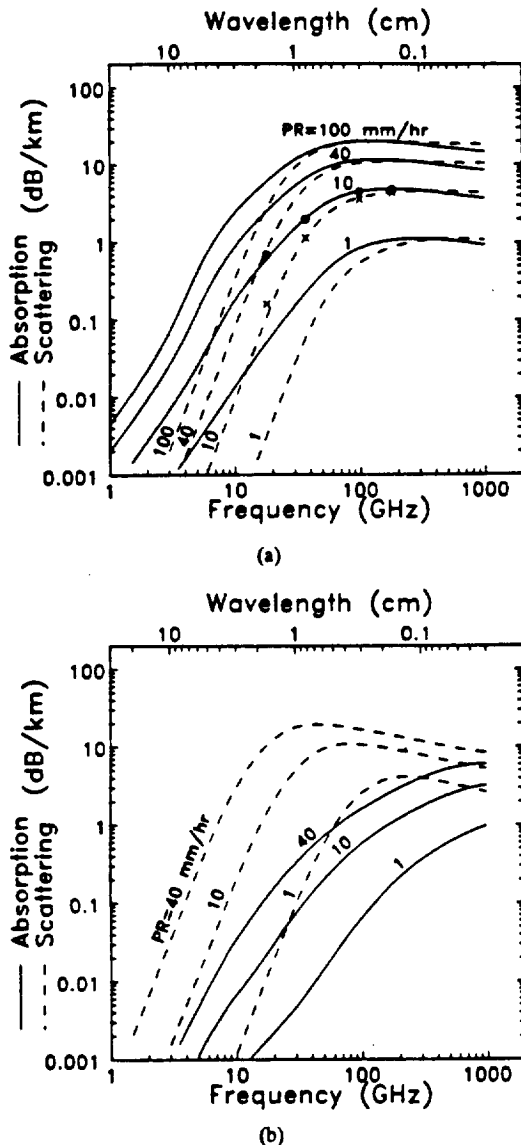


Fig. 2. Polydisperse Mie hydrometeor absorption and scattering (from Gasiewski and Staelin [1]): (a) Liquid, assuming a Marshall-Palmer drop size distribution. Computations from Savage [2] for absorption (—) and scattering (---) are plotted for comparison. (b) Ice, assuming a Sekhon-Srivastava distribution. Calculations are shown for precipitation rates of 1, 10, and 40 mm/h for both phases and 100 mm/h for liquid.

2. Water vapor profiling using 325 GHz spectra,
3. Cloud detection and water content estimation,
4. Precipitation mapping,
5. Observation of additional meteorological degrees of freedom using a wideband channel set.

A new cross-track scanning imaging radiometer for use on the NASA ER-2 and DC-8 aircraft, the Millimeter-wave Imaging Radiometer (MIR), is described. Data from the MIR will be used to verify EHF and SMMW radiative transfer models and demonstrate tropospheric water vapor and cloud parameter retrieval and precipitation mapping using EHF and SMMW channels.

II. SPATIAL RESOLUTION ENHANCEMENTS

Because of the the nonlinear relationship between hydrome-

teor parameters (e.g., rain rate) and brightness temperatures for frequencies above ~ 10 GHz, spatially undersampled imagery can result in ambiguous precipitation parameter retrieval. For example, at 37 GHz, a 50-mm/h oceanic rain cell occupying 10% of a beam footprint produces approximately the same observed brightness as a 1-mm/h drizzle occupying the entire footprint (as can be inferred from [3]), even though the footprint-averaged rain rates differ by a factor of five. Even in the case of passive microwave temperature sounding (which uses a linear retrieval operator), the presence of small undetected precipitation cells can cause substantial brightness perturbations that are indistinguishable from mesoscale temperature fluctuations. If the fractional coverage of precipitation within the footprint is unknown, unacceptable temperature profile retrieval errors can result. Similarly, the presence of undetected clouds is expected to cause unacceptable water vapor profile retrieval errors [4], [5]. Since clouds and rain cells are typically no smaller in horizontal extent than a few kilometers, spatial resolution comparable to this is ultimately desirable for clear-air screening and unambiguous cloud and precipitation measurements.

The subsatellite 3-dB footprint size of a diffraction-limited microwave sensor with aperture diameter D (in m) is:

$$R = 0.38 \frac{h}{fD} \quad (1)$$

where R is the footprint diameter (in km), h is the satellite altitude (in km), f is the frequency (in GHz), and a quadratic aperture field taper is assumed. Footprint sizes of satellite-based microwave imagers such as the NOAA Microwave Sounding Unit (MSU, 110 km at ~ 50 GHz), the Advanced Microwave Sounding Unit (AMSU-B, 15 km at 183 GHz), and the Defense Meteorological Satellite Program (DMSP) Special Sensor microwave Imager (SSM/I, 12.5 km at 85.5 GHz) are larger than the sizes of many clouds and convective precipitation cells. However, from a 1000-km altitude low-Earth orbit, acceptable subsatellite spatial resolutions of $R = 3.5$ and 2.3 km at $f = 220$ and 325 GHz (respectively) could be obtained with a 0.5-m aperture.

High spatial resolution will be particularly difficult to achieve from geosynchronous orbit using conventional microwave channels [6]. As an example, the size of the largest solid aperture-type antenna that can be launched using either the space shuttle or a Titan-IV vehicle is ~ 4.4 m. The smallest footprint size available using a this aperture at 90 GHz is $R = 34.5$ km. However, at 325 and 410 GHz these sizes are $R = 9.5$ and 7.6 km (respectively), and are satisfactory for many hydrological and meteorological requirements [7].

III. WATER VAPOR PROFILING USING 325 GHz SPECTRA

The microwave absorption spectrum of the asymmetric top $^1\text{H}_2^{16}\text{O}$ is caused by rotational transitions induced by the interaction of external fields with the molecule's permanent electric dipole moment. Water vapor resonances at microwave frequencies, in particular 183.310 and 325.153 GHz, are adequately modeled by the Van Vleck-Weisskopf line shape function [8]. Additional microwave absorption contributions

TABLE I
LINE PARAMETERS b_{1i} , b_{2i} , b_{3i} , AND CENTER FREQUENCIES ν_i FOR SEVEN
OF THE MOST SIGNIFICANT H_2O LINES FOR TROPOSPHERIC REMOTE
SENSING, ALONG WITH CONTINUUM PARAMETERS b_f AND b_c [12].

ν_i (GHz)	b_{1i} (kHz/mbar)	b_{2i} —	b_{3i} (GHz/mbar)
22.2351	0.0109	2.143	0.002784
183.3101	0.23	0.653	0.003164
325.1529	0.154	1.515	0.00297
380.1974	1.19	1.018	0.003036
448.0011	1.06	1.370	0.00238
556.9360	51	0.114	0.0030
752.0332	25	0.336	0.00286
$b_f = 1.13 \times 10^{-8}$ (GHz ⁻¹ mbar ⁻²)			
$b_c = 3.57 \times 10^{-7}$ (GHz ⁻¹ mbar ⁻²)			

by water vapor have been hypothesized to arise from the wings of strong H_2O rotational lines located in the far-infrared. In the microwave region, these contributions form a "continuum" that varies slowly with frequency. To date, attempts to model the H_2O continuum absorption using both statistical and impact theories [9] have had limited success. However, extensive empirical characterization of both H_2O continuum and resonant absorption has been done by Liebe [10], whose reduced-line water vapor absorption model [11,12] is adequate for frequencies below 1000 GHz: where ν is in GHz, and $\theta = 300/T$, with T in K. The term in braces is the H_2O contribution (in ppm) to the imaginary portion of the complex air refractivity. The parameters b_{1i} , b_{2i} , b_{3i} , and center frequencies ν_i for the seven most significant H_2O lines for tropospheric and lower stratospheric passive sensing, along with continuum parameters b_f and b_c for the Liebe model are listed in Table I. The parameters of the continuum term depend on the particular set of lines that are included in the reduced summation. The Liebe water vapor absorption model is consistent with clear-air absorption measurements at 337 GHz [13], [14].

From the Liebe model, the 183 and 325-GHz lines are seen to have nearly the same strength and broadening characteristics. Thus, it is expected that satellite- or aircraft-based nadiral observations near the 325-GHz line can be used to profile water vapor in clear-air with essentially the same accuracy as the 183-GHz line. (Profiling in the presence of clouds is discussed in Section VI.) This can be seen by considering the similarity of computed sets of nadiral clear-air weighting functions for channels near 183 and 325 GHz. The weighting functions display the response of the i^{th} channel to the kinetic

temperature $T(h)$ at various atmospheric levels:

$$T_{Bi} = \int_0^\infty T(h') W_i(h') dh' + T_S W_{Si}(f) + T_{CB} W_{CBi}(f) \quad (3)$$

where T_{Bi} is the brightness temperature for the specific passband of the i^{th} channel, and the weights W_{Si} and W_{CBi} are the contributions to the observed brightness from the surface temperature T_S and cosmic background temperature $T_{CB} = 2.7$ K.

Weighting function computations were made using the Liebe water vapor model and the Rosenkranz [15] oxygen absorption model, along with an exponential water vapor profile and the U.S. 1976 mean atmosphere temperature profile [16]. A 2-km water vapor scale height and land background were assumed. Contributions from six SMMW O_2 lines above 368 GHz (as listed by Liebe [11]) are included. Nonresonant N_2 absorption [17] is also included, however, it contributes only a minor amount to the total absorption. Contributions from other constituents are practically negligible for broadband channels (i.e., bandwidths greater than ~ 10 MHz) below 410 GHz. Indeed, H_2O and O_2 are the dominant gaseous absorbers in the troposphere and lower stratosphere at SMMW and lower frequencies.

The computations show that temperature weighting functions for double-sideband channels near $183 \pm 1, 3, 7$ GHz (Figs. 3a and b) are essentially identical to ones near $325 \pm 1, 3, 9$ GHz, and a channel near the 220-GHz transmission window is essentially identical to the 166-GHz channel. Thus, these two channel sets are expected to be equally sensitive to water vapor for purposes of clear-air profiling. This equivalence is further illustrated by the difference between computed nadiral brightness temperature spectra near 183 and 325 GHz for various atmospheric scenarios (Fig. 4). For two disparate relative humidity profiles (20% and 80% surface relative humidity, SRH), the clear-air 183- and 325-GHz spectra are offset by a constant spectrum, suggesting that the difference spectra are nearly independent of the humidity profile. Hence, it is expected that clear-air water vapor profiling can be performed, in principle, equally well using channels near either the 183- or 325-GHz line. Similarly, it is expected that low- to mid-altitude (~ 500 – 800 mbar) water vapor can be probed equally well using channels at either the 166- or 220-GHz transmission windows.

Simulations of the AMSU-B instrument's capabilities suggest that relative humidity retrieval errors as low as 5–10% in the 300–1000 mbar pressure region can be achieved using single-spot 90, 166, and 183-GHz data [18], [19]. The absence

$$\kappa_{H_2O} = 0.1820 \nu \left\{ \sum_{i=1}^{30} S_i \frac{\nu}{\nu_i} \left[\frac{\Delta \nu_i}{(\nu - \nu_i)^2 + \Delta \nu_i^2} + \frac{\Delta \nu_i}{(\nu + \nu_i)^2 + \Delta \nu_i^2} \right] + (b_f P \theta^3 + b_c \theta^{10.5}) e^{\nu} \right\} \quad (\text{dB/km})$$

$$\Delta \nu_i = b_{3i} (P \theta^{0.8} + 4.8 e \theta)$$

$$S_i = b_{1i} e \theta^{3.5} e^{b_{2i} (1 - \theta)}$$

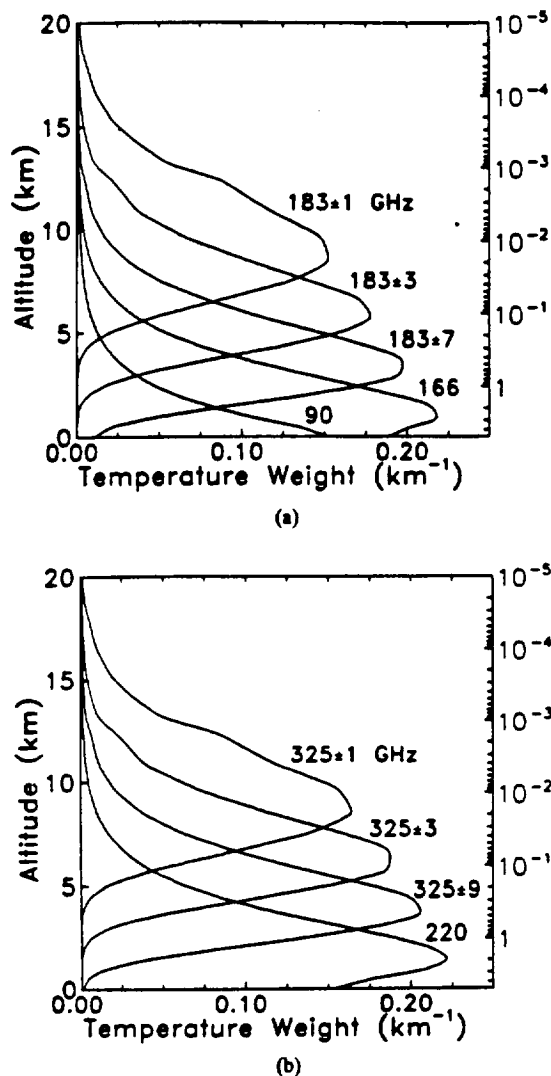


Fig. 3. Clear-air temperature weighting functions vs. altitude for channels at (a) 90, 166, and $183 \pm 1.3.7$ GHz, and (b) 220, and $325 \pm 1.3.9$ GHz. The right-hand ordinate is the approximate water vapor burden.

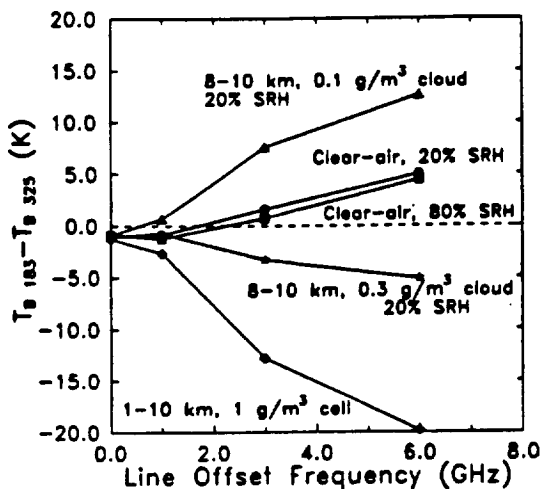


Fig. 4. Computed nadir brightness spectra differences between similar 183- and 325-GHz channels for clear-air (20% and 80% surface relative humidity), clouds (0.1 and 0.3 g/m^3 density, 8-10 km altitude), and precipitation (1 g/m^3 density, 1-10 km altitude).

90 GHz) is a slight drawback. This will somewhat reduce the 220/325-GHz retrieval accuracy in the 800-1000 mbar pressure region, particularly for summer tropical and mid-latitude scenarios. If desired, a 90-GHz channel can be included along with the 220/325-GHz channels to provide low-altitude sensitivity, albeit at degraded spatial resolution.

IV. CLOUD DETECTION AND WATER CONTENT ESTIMATION

Most nonprecipitating clouds consist of hydrometeors of mean volume-equivalent radius $\sim 50 - 100 \mu\text{m}$ and of densities within the range ~ 0.01 to $\sim 0.1 \text{g/m}^3$. Particle phases are generally either pure liquid or layered liquid and ice (as in stratus and cumulus congestus) or pure ice (as in cirrus). At IR and optical wavelengths, most of the constituent hydrometeors have electrical sizes $ka \gg 1$, where $k = \frac{2\pi}{\lambda}$, λ is the wavelength, and a is the volume-equivalent radius. The associated cloud optical depths at IR wavelengths are typically less than 100 m [20]. Thus, direct subceiling probing of nonprecipitating clouds using IR channels is not possible. In addition, these particles behave as Mie scatterers. Hence, passive IR cloud observations exhibit little spectral variation that can be easily linked to parameters of the cloud particle distribution.

However, for frequencies up to ~ 400 GHz, the electrical sizes of nonprecipitating cloud particles are typically less than or near unity. Thus, these particles behave roughly as Rayleigh scatterers and absorbers, and hence exhibit a monotonically increasing frequency dependence in both scattering and absorption coefficients. The dependence is illustrated in Figs. 5(a) and (b), as based on full Mie calculations of the scattering and absorption coefficients for clouds of exponential hydrometeor size distribution [21]. For a cloud with a $50 \mu\text{m}$ mean particle radius, the liquid extinction coefficient increases from $\sim 8 \text{dB-km}^{-1} \cdot \text{g}^{-1} \cdot \text{m}^3$ at 90 GHz to $\sim 40 \text{dB-km}^{-1} \cdot \text{g}^{-1} \cdot \text{m}^3$ at 410 GHz (a factor of ~ 5). From these values, it is expected that nonprecipitating liquid clouds will be increasingly detectable at 90, 166, 220, 340, and 410 GHz, yet will be transparent to a degree suitable for subceiling measurements of cloud parameters. Over the same frequency range, the ice extinction increases from ~ 1 to $\sim 27 \text{dB-km}^{-1} \cdot \text{g}^{-1} \cdot \text{m}^3$ (a factor of almost 30), suggesting that the SMMW channels will be particularly sensitive to ice clouds in comparison to the conventional microwave channels.

The above hypotheses have been investigated by computing the nadir brightness temperature changes (relative to clear-air) caused by a 2-km thick cloud of varying density, base altitude, latitude, and season. Computations use the iterative radiative transfer model described by Gasiewski [1], applicable for a planar-stratified Mie scattering atmosphere consisting of liquid-, ice-, and mixed-phase clouds. Hydrometeor scattering and absorption are modeled by Marshall-Palmer (MP) and Sekhon-Srivastava (SS) distributed [22], [23] liquid or ice phase Mie spheres with Henyey-Greenstein (HG) phase functions. Two disparate temperature profiles derived from a seasonal and latitudinal interpolation to the 1976 supplemental U.S. standard atmosphere listing are used: January at 90°N latitude (polar winter) and July at 30°N latitude (subtropical

of a low-altitude sensing SMMW channel (comparable to

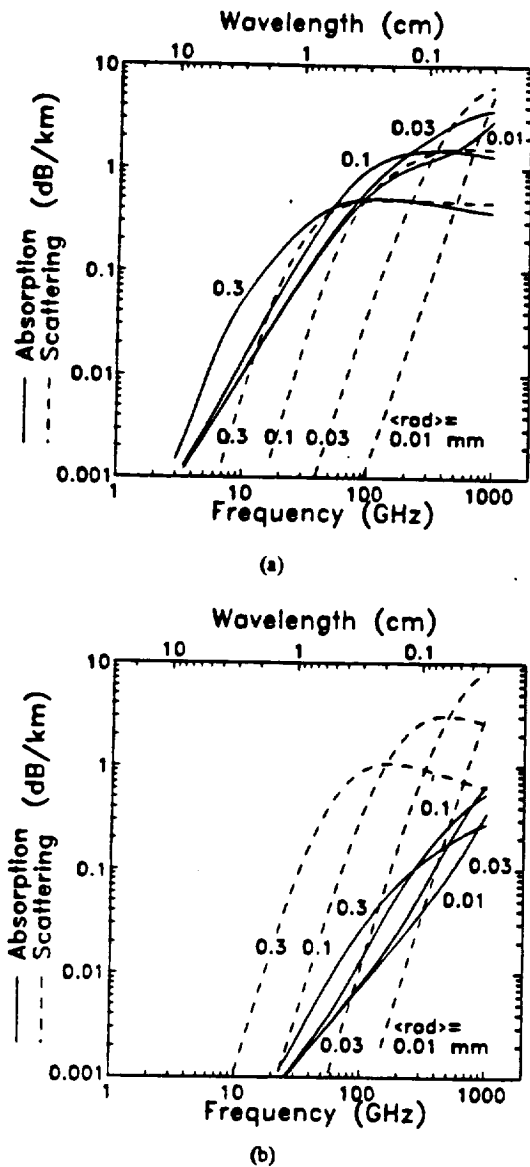


Figure 5: Polydisperse Mie hydrometeor absorption and scattering for a 0.1 g/m^3 cloud of (a) liquid and (b) ice, assuming exponential size distributions. Calculations are shown for average particle radii (rad) of 0.01, 0.03, 0.1 and 0.3 mm at 0°C .

summer). The relative humidity is nominally 40% at the surface, with a 2-km exponential scale height. However, within cloud layers, the water vapor partial pressure is adjusted to equal the saturation vapor pressure ρ_{sat} , the determination of which is based on the temperature T and the mass fraction f_l of total cloud water in the liquid phase:

$$\rho_{\text{sat}}(T, f_l) = f_l \rho_{\text{sat},l}(T) + (1 - f_l) \rho_{\text{sat},i}(T) \quad (4)$$

Cloud densities range from 0.003 to 0.1 g/m^3 and the cloud base-altitude is either 6 or 8 km. The strong 424.763-GHz O_2 line cools the 410-GHz window brightness temperature by $\sim 1 \text{ K}$, and hence is included in the absorption calculation.

The results of the numerical calculations are shown in Figs. 6(a–c), where a land background with 5% reflectivity has been

used. For polar winter conditions (dark circles), all cloud water will be in the ice phase. Under these conditions, the highest frequencies considered (340 and 410 GHz) provide the greatest sensitivity to cloud water, exhibiting negative perturbations of up to 40 K (solid lines) for 0.02 g/cm^2 ice integrated water density (IWD). By assuming the ice cloud detection threshold to be $\sim 1 \text{ K}$ (the single-spot sensitivity of a typical satellite-based radiometer), the minimum detectable ice IWD is $\sim 0.001 \text{ g/cm}^2$. This is approximately five times more sensitive than at 90-GHz.

However, random brightness perturbations of $\pm 3 - 4 \text{ K}$ at 340 or 410 GHz can be expected due to variations in atmospheric water vapor content. These variations can be parameterized by changes in the surface relative humidity (Figs. 6(d–e), dashed lines, dark circles). Since clear-air zenith transmissivities at 340 and 410 GHz are 75% and 55%, respectively, random variations of $\pm 3\%$ in the surface emissivity will produce additional brightness perturbations of $\pm 5 - 6 \text{ K}$. In order to unambiguously detect clouds in the presence of both water vapor and surface variations, the cloud detection threshold must be increased from $\sim 1 \text{ K}$ to $\sim 8 - 10 \text{ K}$. In this case, the minimum detectable IWD using 340 or 410 GHz rises to $\sim 0.004 \text{ g/cm}^2$. At 90 GHz, brightness perturbations due to water vapor variations are negligible, but those caused by variations of up to $\pm 3\%$ in surface emissivity will be somewhat larger ($\pm 7 \text{ K}$) due to the reduced zenith opacity. For unambiguous detection, the minimum detectable ice IWD at 90 GHz rises to $\sim 0.02 \text{ g/cm}^2$. Thus, even when water vapor and surface emissivity variations are considered, the SMMW sensitivity to ice IWD for polar winter conditions is approximately a factor of five greater than at 90 GHz.

For subtropical summer conditions (open circles), cloud water can be liquid, ice, or mixed phase, depending on altitude. For the 8-km base-altitude cloud, virtually all cloud water is frozen. However, for the 6-km base-altitude cloud, an appreciable fraction of the column ($\sim 55\%$) is liquid. At 90 GHz, the larger extinction coefficient of cloud liquid (relative to ice) causes the lower altitude (6 km, mixed-phase) cloud to be more easily detected than the high-altitude (8 km, ice-phase) one (Fig. 6a). Conversely, at higher frequencies (e.g., 166, 220, 340, and 410 GHz), two separate effects allow for easier detection of the higher-altitude cloud: (1) The single-scattering albedo of ice is significantly larger than liquid. Thus, the ice cloud top is more reflective than the ice-liquid cloud, and (2) the opacity of the increased water vapor burden between the satellite and the lower-altitude cloud top is greater. Thus, the response to the lower cloud is diminished. The latter effect is referred to as “water vapor screening.” Channels from 166 to 410 GHz are well suited to detecting high-altitude ice clouds due to an absence of water vapor screening. Lower-altitude liquid and mixed-phase clouds are also detectable at 166–410 GHz, but the advantage in sensitivity relative to 90 GHz is expected to be completely lost for cloud tops below $\sim 4 - 6 \text{ km}$ from screening. The greatest sensitivity to subtropical summer clouds of arbitrary altitude is expected at $\sim 220 \text{ GHz}$. The greatest invariance to cloud altitude (i.e., cloud water phase) is expected at $\sim 166 \text{ GHz}$.

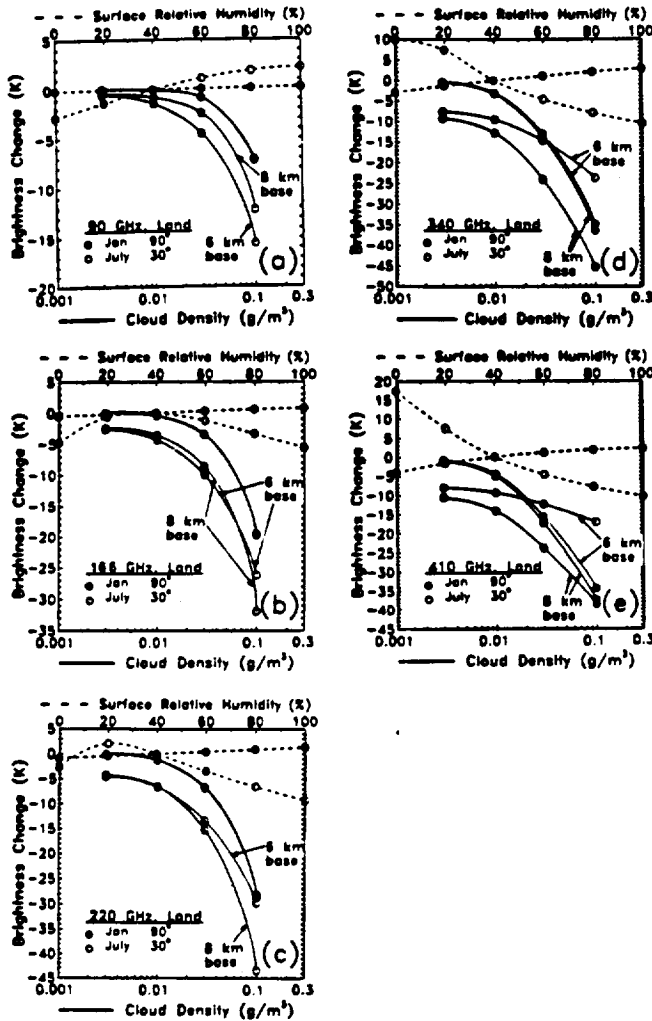


Figure 6: Computed nadir brightness changes due to non-precipitating clouds (solid lines) and water vapor (dashed lines) at (a) 90, (b) 166, (c) 220, (d) 340 and (e) 410 GHz. Open circles are for a subtropical summer atmosphere (July, 30° N latitude) and dark circles are for a polar winter atmosphere (January, 90° N latitude). Clouds are 2 km thick with base altitudes at either 6 or 8 km.

Neglecting water vapor and surface emissivity variations, the minimum detectable IWD's for high-altitude (8-km base altitude) subtropical-summer ice clouds are comparable to those found for the polar winter case. However, for unambiguous cloud detection in the presence of water vapor and surface variations, the subtropical-summer detection thresholds must be increased to $\sim 10 - 25$ K, depending on the channel frequency. In this case, the minimum detectable IWD rises to $\sim 0.1 - 0.15$ g/cm² for any of the channels from 90 to 410 GHz, and the sensitivity advantages of the high frequency channels (166–410 GHz) appear to be lost. However, these advantages can be recovered if the water vapor distribution can be independently measured, as discussed in Section VI. Note that for subtropical summer conditions, the 340 and 410 GHz channels are highly insensitive to variations in either surface temperature or emissivity.

The analysis over an ocean background modeled by a smooth Fresnel-reflecting surface yields similar results. Here, the surface reflectivity is 30–45% at 90 GHz, but decreases to 15–25% at 340 GHz. At the high EHF and SMMW frequencies, this is only slightly greater than for the case of land, hence the resulting cloud sensitivities are nearly identical.

Any differences are even further reduced by ocean foam coverage. In contrast, the sensitivity to clouds at 90-GHz is significantly affected by the highly reflecting ocean surface. Not only is the brightness cooling caused by scattering ice clouds reduced, but a brightness warming caused by absorbing water clouds becomes observable. Although this bimodal effect complicates comparisons between oceanic cloud water sensitivities at 90 and 340 GHz, it appears that the sensitivity advantages of the SMMW channels that have been shown over land are only further enhanced over ocean.

It is also recognized that random surface and atmospheric temperature variations can produce brightness perturbations comparable to those caused by surface emissivity variations. However, the effects of surface and atmospheric temperature variations are expected to be more easily correctable than those of surface emissivity. Indeed, ocean surface temperature is a slowly varying process that can be determined to within $\sim 1^\circ\text{C}$ by a combination of shipborne measurements, satellite measurements, and climatology. In addition, an increase in ocean temperature causes the Fresnel ocean emissivity at EHF and SMMW frequencies to decrease, thereby partly cancelling the effects of the temperature increase on the overall emission. Soil temperatures and vegetation-covered surfaces are highly variable on a diurnal time scale, but exhibit correlations with lower-tropospheric temperatures; both surface and tropospheric temperatures are observable to within $\sim 1 - 3$ K by passive microwave sensors operating at lower frequencies [24], [25]. For all of these surfaces, the impact of residual surface temperature variations on cloud detection capabilities should be minimal. Variations in the temperatures of wet soil and vegetation-, snow- and ice-covered surfaces are slightly more difficult to characterize. However, upon correction, their impact on the cloud detection thresholds should not dominate over those of surface emissivity. Overall, the assumption of a maximum surface emissivity error of $\pm 3\%$ justifies neglecting surface temperature variations when corrections are used.

The preceding discussion assumes that the responses of the SMMW channels to IWD are independent of the actual thickness of the cloud. Indeed, for a given (fixed) hydrometeor size distribution, this assumption is well founded, as illustrated by the computed brightness perturbations for a subtropical summer cloud with a middle-altitude of 7.5 km, a constant IWD of 2.0 g/cm², and thickness varying from 0.5 to 4.0 km (Table II, case "a", using MP and SS mean sizes for 0.1 g/m³ density). Here, the variation in the SMMW brightness perturbation remains below $\pm 14\%$ of its average as the thickness is varied, suggesting that IWD can be accurately measured. Of course, only the IWD within the top one to two optical depths can be directly probed. If the hydrometeor size distribution is allowed to vary with density (case "b", using the MP and SS size relations), the resulting SMMW brightness perturbations vary over $\pm 44\%$ of their average. It is concluded that an independent measurement of mean hydrometeor particle size appears to be required for unambiguous IWD measurements. The potential for such a measurement using a widely spaced set of SMMW channels is discussed in Section VI.

The cloud model used in this section assumes a linearly

23

TABLE II
BRIGHTNESS PERTURBATIONS FOR A 7.5-KM ALTITUDE SUBTROPICAL SUMMER CLOUD OF VARYING THICKNESS AND FIXED INTEGRATED WATER DENSITY (LIQUID AND ICE) OF 2.0 g/cm². CALCULATIONS ASSUME MEAN HYDROMETEOR SIZES THAT ARE (A) FIXED, AT THE MP/SS VALUES FOR 0.1 g/m³ DENSITY, AND (B) VARYING WITH DENSITY, ACCORDING TO THE MP/SS RELATIONS

Size Distribution	Mean Liquid Radius	Mean Ice Radius	Cloud Thickness	Brightness Decrease (K) at Frequency (GHz):				
	(mm)	(mm)		90	166	220	340	410
Clear-air: no cloud				0	0	0	0	0
(a)	0.125	0.126	0.5	-14.3	-26.7	-30.5	-25.3	-18.5
(a)	0.125	0.126	1.0	-14.5	-27.2	-31.2	-25.9	-19.1
(a)	0.125	0.126	2.0	-14.7	-28.2	-32.4	-27.4	-20.8
(a)	0.125	0.126	3.0	-15.0	-29.2	-33.7	-29.2	-22.6
(a)	0.125	0.126	4.0	-15.1	-30.1	-34.8	-30.9	-24.4
(b)	0.177	0.261	0.5	-16.1	-21.8	-21.1	-14.4	-10.2
(b)	0.149	0.182	1.0	-16.0	-25.9	-27.2	-20.2	-14.7
(b)	0.125	0.126	2.0	-14.7	-28.2	-32.4	-27.4	-20.8
(b)	0.113	0.102	3.0	-13.7	-28.7	-34.5	-31.9	-25.1
(b)	0.105	0.088	4.0	-12.8	-28.6	-35.5	-35.1	-28.7

mixed phase between the freezing level and the altitude of ice nucleation (assumed to be -30°C). While this is an accepted model for precipitating clouds, the mixed phase is unusual in nonprecipitating clouds. Here, the Bergeron-Findeisen process rapidly depletes the liquid phase, resulting in precipitating ice that subsequently liquifies upon descent. However, insofar as passive sensing is concerned, the effects of a mixed-phase cloud are similar to those of a two-layer ice-over-liquid cloud. Such a two-layer cloud does not exhibit Bergeron formation, and is thus relatively stable. The reason for the radiometric similarity is that passive EHF and SMMW observations are not extremely sensitive to the precise height of partially opaque layers of hydrometeors. Thus, for the purposes of this section, it is appropriate to use the linearly mixed-phase model. If the mixed-phase region were deleted from the model, then the proper choice of ice nucleation temperature becomes important. By choosing 0°C , the model becomes biased toward strongly-scattering ice clouds. By choosing -30°C , the model becomes biased toward absorbing supercooled liquid clouds. While uncommon in nature, the mixed-phase cloud model effectively sets the ice nucleation temperature in between these extremes.

V. PRECIPITATION MAPPING

Channels at 220, 340, and 410 GHz are more sensitive to clouds than the conventional EHF channels, although they are not as sensitive as IR channels, and are not expected to exhibit brightness temperature saturation for many cases of convective and stratiform precipitation. To demonstrate, brightness temperatures over simulated heavy clouds and raincells have been computed using the iterative numerical model for the high-frequency window channels 90, 166, 220, 340, and 410 GHz (Fig. 7). The computations used the iterative method, assuming MP liquid spheres, SS ice spheres, and HG phase functions with the total hydrometeor density uniform

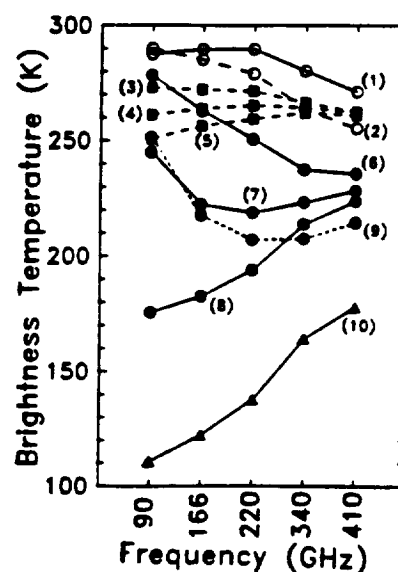


Fig. 7. Computed window-channels nadir brightnesses over heavy clouds and convective precipitation: (1) clear-air, 20% surface relative humidity, (2) clear-air, 80% surface relative humidity, (3) 4–6 km, 0.1 g/m³, MP liquid cloud layer, (4) 4–6 km, 0.3 g/m³, MP liquid cloud layer, (5) 1–6 km, 1 g/m³ MP-SS cell, (6) 8–10 km, 0.1 g/m³, SS ice cloud layer, (7) 8–10 km, 0.3 g/m³, SS ice cloud layer, (8) 1–10 km, 1 g/m³ MP-SS cell, (9) 8–10 km, 0.3 g/m³, MP ice cloud layer, (10) 1–14 km, 1 g/m³ MP-SS cell.

over the indicated altitude regions. The temperature profile is interpolated from the U.S. standard atmosphere listings for July at 35°N latitude, and the temperature of ice nucleation is -30°C . An exponential water vapor decay with a 2-km scale height and 20% nominal surface relative humidity, and a land background with 5% reflectivity is assumed. The accuracy of the model has been verified for a case of mature convective precipitation using nadir 118-GHz spectra [1]. The model also yields results that are consistent with a numerical microwave radiative transfer model currently used at the NASA Goddard Space Flight Center [26].

Several scenarios are displayed in Fig. 7: moist and dry clear-air (curves 1 and 2), and both low- and high-altitude

clouds (curves 3, 4, 6, 7, and 9) and precipitation (curves 5, 8, and 10). The hydrometeor density varies from 0.1 to 1.0 g/m³, corresponding to MP precipitation rates of ~ 1–18 mm/hr, respectively. As shown by Adler *et al.* [27] using coincident microwave and IR data, an IR channel would be expected to saturate over any of the hydrometeor-laden scenarios (3–10) in Fig. 7 (see also [28]). Conversely, microwave channels at 92 and 183 GHz have been shown to contain useful information on the underlying storm structure and rain rate (see, e.g., [29]).

From Fig. 7, the response of the SMMW channels (340 and 410 GHz) relative to the conventional channels can be predicted. Over the eight cloud and raincell scenarios, the expected brightness variation of a SMMW channel is approximately one-third to three-fourths that of a 90-GHz channel. Further, the sensitivity of a SMMW channel to precipitation will be suppressed relative to 90-GHz, and the sensitivity to thin (nonprecipitating) clouds will be enhanced. Overall, the SMMW channels will be somewhat less sensitive to storm structure and rain rate than at 90-GHz, but more sensitive to the presence of ice canopies.

The computed weighting functions for absorbing and scattering hydrometeor-laden atmospheres at 90- and 340-GHz (Figs. 8(a) and (b)) help explain these sensitivity differences. Two features are essential in determining the upwelling brightness: the weighting function peak-altitude and the cosmic background weight W_{CB} (the background weight is essentially equal to the cell top reflectivity since little reflection occurs via the land surface). At low ice densities (< 0.3 g/m³, or ~ 1 mm/hr SS ice precipitation rate), scattering and absorption at 340 GHz (Fig. 2(b)) cause up to 20% cell top reflection, along with a high-altitude (~ 8–10 km) weighting function peak. Both of these effects produce a cooling in the upwelling brightness, although the mechanism of cell top reflection, rather than emission from colder levels, is dominant. At higher ice densities, the 340-GHz single-scattering albedo decreases slightly, effectively saturating the cell top reflectivity. Any further decreases in 340-GHz brightness are due primarily to increases in the cell-top opacity, which further attenuate radiation originating from warm low altitudes.

At 90 GHz, ice scattering is insignificant until a critical density of ~ 0.5 g/m³ is exceeded. Such a critical value arises due to a strong nonlinearity between cloud density and the volume scattering coefficient: as cloud density increases, so does the mean cloud particle size. For Rayleigh scatterers, this causes an abrupt increase in the scattering coefficient (as illustrated by Fig. 5(b)). Thus, the 90-GHz brightness exhibits little change at lower densities. At higher densities, the cell is radiometrically opaque [1]: The weighting function peaks within the ice layer, and the reflectivity rapidly increases with density. However, in this case the 90-GHz ice single-scattering albedo does not significantly decrease with increasing density. Thus, at densities greater than ~ 0.5 g/m³, the 90-GHz cell top reflectivity exceeds that at 340 GHz by several percent, and the resulting brightness temperature does not saturate for typical cell densities.

Screening by water vapor above the cell top contributes further to reduced sensitivity at 340 GHz relative to 90 GHz.

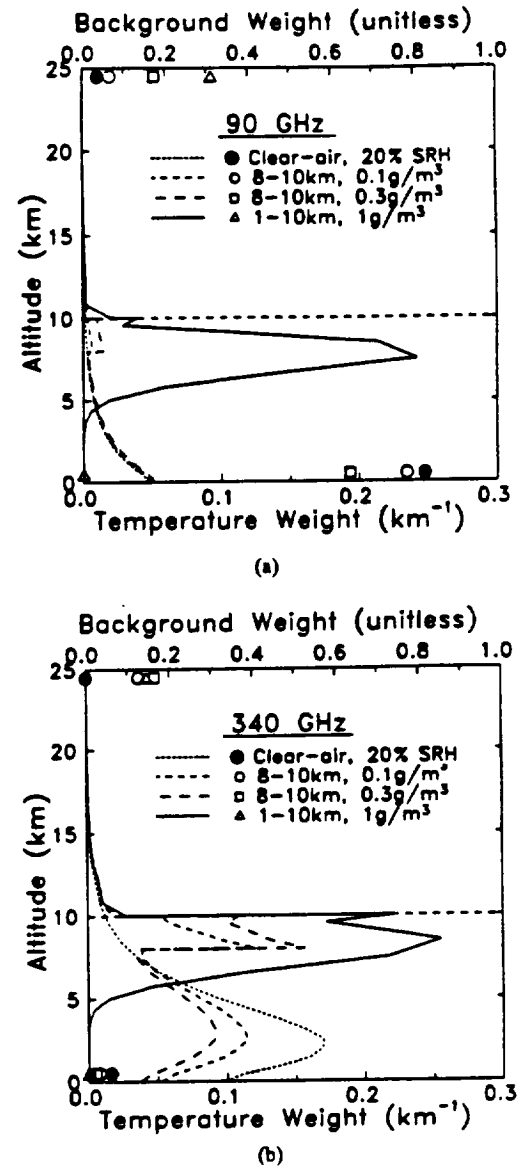


Fig. 8. Computed nadir temperature weighting functions at (a) 90 GHz and (b) 340 GHz for clear-air, clouds, and precipitation. The symbols near 0 and 25 km indicate the surface and cosmic background contributions, respectively.

By considering the summer low-latitude atmospheric profile in Fig. 7, the extreme effects of water vapor screening on SMMW observations are displayed. For example, curves 3–5 show the window-channel response to low-altitude (6 km cell top) liquid precipitation. Although the liquid drops cause significant scattering and absorption at SMMW frequencies, variations in brightness are screened by intervening water vapor. For high-altitude cells, the screening opacity is small (curves 6–8, 10), and the resulting variations in the SMMW channels are significantly greater. For these scenarios, the SMMW channels will not saturate, and can provide useful information on storm structure, heavy clouds, and precipitation for many scenarios in which IR channels would saturate. Precipitation cell cores should be detectable at 220-, 340-, and 410-GHz beneath many optically opaque (0.01–0.05 g/cm²) cirrus canopies. By virtue of their potential for enhanced spatial resolution, such channels would be particularly useful for precipitation mapping and

resolving ambiguities caused by fractional footprint-filling in 10-, 18-, and 37-GHz images of oceanic rain rate. At high-latitudes or during winter conditions, the screening opacity due to water vapor will be considerably lower, and the SMMW channels will be particularly useful for detecting and mapping both high- and low-altitude precipitating clouds.

For radiometrically opaque cells (i.e., $W_S \approx 0$), the cell probing depth is the distance down into the cell over which most emission occurs. This defines a region which comprises most of the weighting function's area below the cell top. Below this region, no direct radiometric observations of hydrometeor parameters can be made. Under most conditions, the SMMW channels will not be able to directly probe surface rain rate. However, indirect information on low-level rainrate might be inferred statistically from correlations with direct radiometric observations of other raincell parameters, e.g., the cell's size and altitude [30], [31]. In addition, the monotonic decrease of cell probing depth with increasing frequency suggests that hydrometeor parameter profiling in heavy clouds and precipitation cell tops might be facilitated using conventional channels along with a widely spaced set of SMMW channels. The concept of passive precipitation profiling has been discussed by Kummerow [29].

VI. ADDITIONAL METEOROLOGICAL DEGREES OF FREEDOM THROUGH WIDEBAND OBSERVATIONS

The enhanced sensitivity to ice clouds at 220 and 325 GHz is a deterrent for water vapor profiling. However, it is expected that by using these channels in conjunction with the conventional channels (90, 166, and 183 GHz), additional meteorological information (not obtainable using either of these bands exclusively) can be obtained.

Support for this notion arises from nadir aircraft observations at 60 and 118 GHz [1], [32]. The data has revealed that perturbations caused by clouds and light precipitation are typically 2–3 times as large in the 118-GHz channels as compared to corresponding 60-GHz channels (i.e., those with similar clear-air weighting functions). The observed sensitivity differences have been corroborated by calculations using the iterative radiative transfer model, and are due to Rayleigh scattering and absorption by the electrically small hydrometeors. Thus, coincident observations of clouds and light precipitation using similar 60 and 118-GHz channels results in an additional degree of freedom related to liquid and ice water content, although it is not clear at this time how to best use this information. Over heavy precipitation, the scattering and absorbing hydrometeors are electrically large. In this case the coincident 60 and 118-GHz perturbations are comparable, and provide no additional information.

Analogously, at least one additional degree of freedom is expected using similar channels near the 183- and 325-GHz H_2O lines. Due to the Rayleigh frequency dependence of small (< 0.1 mm diameter) hydrometeors, these channels will respond differently to layers of nonprecipitating cloud. Referring again to Fig. 4, a thin ice cloud layer (8–10 km, 0.1 g/m^3) perturbs channels near 325 GHz more strongly than near 183 GHz (nearly a 15-K difference), suggesting

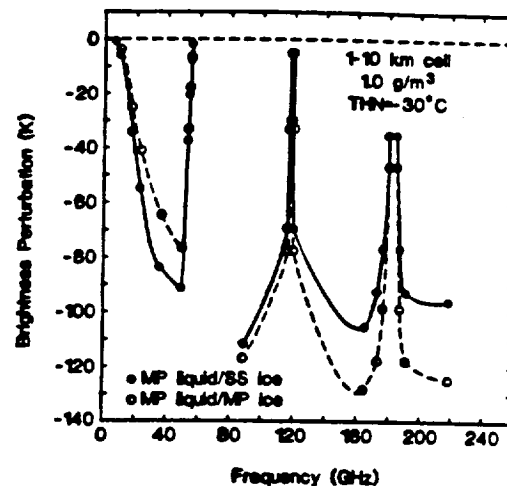


Fig. 9. Nadir brightness perturbation spectra for a model 1–10 km, 1.0 g/m^3 precipitation cell. The calculations were made using the iterative planar-stratified numerical model for two ice particle size distributions: Marshall–Palmer (MP) and Sekhon–Srivastava (SS).

that information concerning the presence of the thin cloud is available from the difference spectra between these two bands. This information can potentially be used to correct water vapor soundings, and is only available from coincident observations at both 183 and 325 GHz. As the cloud density increases (8–10 km, 0.3 g/m^3 cloud layer and 1–10 km, 1 g/m^3 cell), the sign of the trend in Fig. 4 reverses, and the 183-GHz channels are more strongly perturbed (nearly a -20 K difference). The bimodal sensitivity is a consequence of the transition from Rayleigh to Mie scattering as the hydrometeor density (and hence size) increases. For frequencies below the Rayleigh-Mie transition peak (Figs. 2(a) and (b)), scattering and absorption increase with frequency. Above this peak, scattering by ice and both scattering and absorption by liquid decrease slowly with frequency.

Another example of an additional degree of freedom is illustrated in Fig. 9. Computed brightness perturbation spectra over a rain cell using a wideband channel set are shown for two different ice size distributions: MP and SS. The model cell density is 1 g/m^3 and extends from 1 to 10 km in altitude. The temperature of ice nucleation is -30°C . The MP-distributed ice spheres (which are typically smaller than SS-distributed spheres for densities near 1 g/m^3) cool the brightness spectrum at the higher EHF frequencies (90, 118, 166, 183, 220 GHz) and increase the brightness spectrum at lower frequencies (6, 10, 18, 22, 37, and 60 GHz). Thus, the brightness perturbation spectrum “pivots” around a frequency near 75 GHz. The slope of this spectrum, as measured using a widely spaced channel set, contains information on the particle size distribution.

For a wideband EHF and SMMW channel set, a similar degree of freedom related to cloud ice particle size might be expected. This is illustrated in Fig. 7 (curves 7 and 9), for a 2-km thick, 0.3 g/m^3 ice layer. Here the computed window channel spectrum also pivots as the ice size distribution is changed from SS to MP, but around a frequency of ~ 140 GHz. The change reduces the mean ice radius from ~ 0.22 mm to ~ 0.16 mm, which subsequently increases the 166,

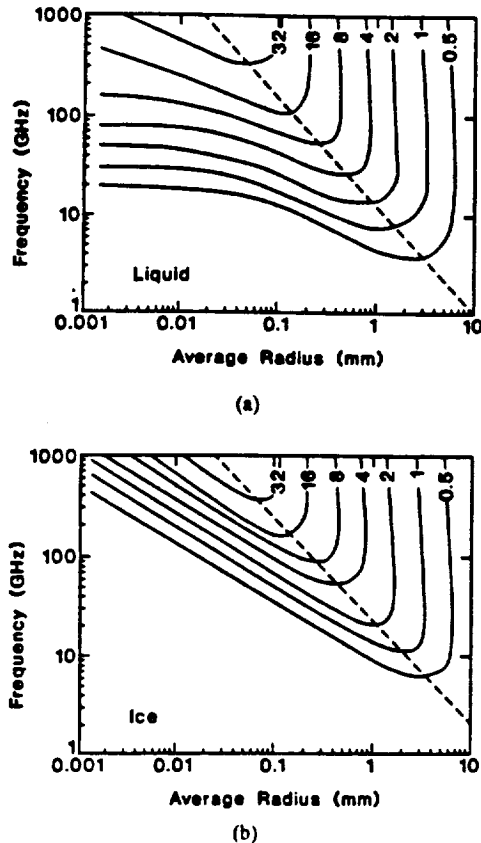


Fig. 10. Extinction contours for exponentially-distributed Mie (a) liquid and (b) ice spheres. Contour values are in $\text{dB}\cdot\text{km}^{-1}\cdot\text{g}^{-1}\cdot\text{m}^3$. Along the dashed lines, the sensitivity of extinction to variations in mean hydrometeor size vanishes.

220, 340, and 410 GHz scattering coefficients, thereby cooling the high-frequency portion of the spectrum. Simultaneously, scattering is slightly decreased at 90 GHz, thereby warming the low-frequency portion.

Generalizing, we can define the spectral pivot frequency f_p as the frequency at which the hydrometeor extinction exhibits minimum sensitivity to mean hydrometeor size:

$$\frac{\partial \kappa_e}{\partial \langle a \rangle} \approx 0 \quad (5)$$

From the preceding discussion, it appears that $f_p \approx 32/\langle a \rangle$, where a is in millimeters and f_p is in gigahertz. This is in general agreement with relationships determined graphically using constant-extinction contours (Figs. 10(a) and (b)), where it is seen (dashed lines) that $f_p \approx 15/\langle a \rangle$ for liquid and $f_p \approx 25/\langle a \rangle$ for ice. In either case, f_p is slightly below the Rayleigh-Mie transition frequency, and results from the scattering peak near this frequency.

The sensitivity to size distribution displayed by the perturbation spectra in Figs. 7 and 9 suggest an observable mode which is related to the mean ice particle size. Indeed, the slope of the brightness spectrum near f_p is sensitive to the mean hydrometeor size, and thus might potentially be useful for such measurements. Due to the inherent lack of structure in microwave hydrometeor scattering and absorption spectra, a widely-spaced window-channel set (preferably spanning at least one octave) with high spatial resolution (to eliminate footprint-filling ambiguities) would be required to observe this

hypothesized hydrometeor size degree of freedom. The EHF and SMMW window channels from 90 to 410 GHz are well suited for this task.

Brightnesses near f_p exhibit minimum sensitivity to hydrometeor size variations, and thus should be useful for measurements of other cell parameters such as IWD. For many nonprecipitating clouds, f_p is between $\sim 200 - 600$ GHz, suggesting that the SMMW channels 220, 340 and 410 GHz are particularly well suited for nonprecipitating cloud IWD measurements.

VII. THE MILLIMETER-WAVE IMAGING RADIOMETER (MIR)

The Millimeter-Wave Imaging Radiometer (MIR) is a new instrument being designed for studies of airborne passive microwave retrieval of tropospheric water vapor, clouds, and precipitation parameters [33]. The MIR is a total-power cross-track scanning radiometer for use on either the NASA ER-2 (high-altitude) or DC-8 (medium altitude) aircraft. The current design includes EHF channels at 89, 150, 183, ± 1.3 , 7, and 220 GHz, and SMMW channels at 325 ± 1.3 , and 9 GHz. Identical 3.5° beamwidths for all channels produce nadir footprint sizes of ~ 700 m at mid-altitude (~ 10 km) when operated aboard the NASA ER-2 (the cruise altitude of the ER-2 is ~ 20 km). The $\pm 50^\circ$ field-of-view is scanned every ~ 2.9 s.

The current MIR design consists of a scanhead and data acquisition system, designed for installation in the ER-2 superpod nose cone. The scanhead will house the receivers (feedhorns, mixers, local oscillators, IF amplifiers, and video detectors), a scanning mirror, hot and cold calibration loads, and temperature sensors. The data acquisition system is to consist of a 80286-based computer with 1000 MB tape drive, a 12-b 48-channel opto-isolated A/D converter, 8-b D/A converter (for offset drift compensation) and a power supply/conditioning module. Software-controlled offset and gain adjustments will compensate for expected receiver gain and noise temperature fluctuations.

The high spatial resolution EHF and SMMW brightness imagery will be useful for:

- (1) Verifying EHF and SMMW radiative transfer models in clear air, clouds and precipitation, with direct comparisons at frequencies up to 334 GHz,
- (2) constructing and evaluating EHF and SMMW mapping and retrieval algorithms for precipitation parameters (e.g., rainfall rate, particle size, and cell-top altitude), cloud parameters (e.g., liquid and ice water content, and particle size), and water vapor profile retrievals. Of particular interest are potential measurements of cirrus ice water content, and evaluation of the 325-GHz water vapor line for spaceborne profiling of tropospheric water vapor. In addition, the imagery will be useful for:
- (3) studying convective raincell and atmospheric gravitational wave structure,
- (4) evaluation of passive microwave satellite data from instruments such as AMSU-B and SSM/T2, and

5. (5) development of techniques for combining observations at EHF and SMMW channels along with IR and conventional microwave channels to facilitate the estimation of temperature and water vapor profiles, and precipitation parameters, particularly ice density and ice size distributions.

Many of the MIR science objectives will require complementary data from other airborne, ground-, and satellite-based instruments (e.g., imaging radiometers operating at complementary frequencies, ground-based and airborne doppler weather radars, satellite- and airborne optical and infrared imagers, and radiosondes).

VIII. DISCUSSION

In this paper, we have outlined the chief advantages and disadvantages of passive EHF and SMMW channels as applied to satellite-based tropospheric and lower stratospheric remote sensing. Briefly, the following conclusions are drawn concerning these largely unexplored channels:

(1) Enhanced spatial resolution from diffraction-limited antennas of practical size is available using the SMMW channels.

(2) Channels around the 325-GHz water vapor line and in the 220-GHz window can be used for water vapor profiling in clear air with an accuracy comparable to that expected using 166 and 183-GHz channels. However, with no additional information, the adverse effects of clouds will be greater.

(3) Clouds can be detected using 340 or 410 GHz at densities as low as 0.004g/cm^2 , particularly under polar winter conditions or at altitudes greater than ~ 6 km. The available sensitivity to clouds increases significantly with frequency above 90 GHz. Thus, the SMMW channels are expected to be useful for imaging cirrus and nonprecipitating cumulus structure. For subtropical summer clouds under $\sim 4 - 6$ km altitude, 90, 166, and 220 GHz appear best for detection and IWD measurement.

(4) Many heavy clouds and precipitation can be mapped using SMMW channels with one-third to three-fourths of the brightness variation expected using 90 GHz. Saturation, as exhibited in IR imagery of rain cells, is not often expected. Images of cirrus clouds using SMMW channels and raincells might potentially facilitate the indirect retrieval of surface rain rate using other low-frequency microwave channels (e.g., 10, 18, and 37 GHz). However, contrast reduction due to water vapor screening will be significant for cells with low top-altitudes (~ 6 km or less) during subtropical summers.

(5) Additional meteorological degrees of freedom related to water vapor, cloud integrated water density, and mean particle size are expected using a wideband set of EHF and SMMW channels. For unambiguous detection of clouds under summer subtropical conditions, independent information on the water vapor profile will be required. This could potentially be obtained from such a wideband set. It also appears possible that a wideband set of EHF and SMMW channels (e.g., 90, 166, 220, 340, and 410 GHz) can be used to retrieve both cloud integrated water density and mean hydrometeor size.

Major deterrents to developing meteorological retrieval algorithms using EHF and SMMW passive channels are the nascent states of radiative transfer science and the lack of experimental radiometric imagery for microwave frequencies above 200 GHz. Meteorological data flights of the MIR aboard the NASA ER-2 along with subsequent data analyses will be crucial in refining radiative transfer models (particularly for cirrus clouds) and in developing EHF and SMMW retrieval algorithms. The first MIR data flights occurred in 1992, and future flights are planned for 1993 in conjunction with TOGA/COARE. Measurements of mean ice particle size and cloud IWD could provide useful information on the infrared radiative properties of cirrus clouds; these results could have an impact on the role of cirrus in global warming and links between cirrus clouds and precipitation. Currently, cirrus cloud radiative properties are a major source of uncertainty in global radiation and climate models.

We specifically have not addressed the issues of nascent SMMW receiver and antenna technology, or the increased integration noise expected for high-resolution SMMW observations due to reduced spot dwell time. Indeed, enhanced spatial resolution using a single-beam scanning imager can be gained only at the expense of reduced spot integration time, and hence increased radiometric noise. However, such increases can potentially be offset by using multiple scanning beams, wider IF bandwidths, longer scene revisit times, and improvements in receiver sensitivity. Reflector surface accuracies of $10\mu\text{m}$ or less are acceptable up to 410 GHz, and are technologically feasible for spaceborne antennas several meters in diameter. It is (somewhat tacitly) assumed that these and other associated problems are surmountable through future improvements in radiometer and large space structure technology. However, careful absolute calibration and high radiometric resolution will be required to observe any wideband spectral modes.

ACKNOWLEDGMENT

The author thanks Dr. R.F. Adler of the NASA Goddard Space Flight Center for collaborative discussions. Thanks are also due to the reviewers for their thoughtful queries.

REFERENCES

- [1] A. J. Gasiewski and D. H. Staelin, "Numerical modeling of passive microwave O_2 observations over precipitation," *Radio Sci.*, vol. 25, no. 3, pp. 217-235, 1990.
- [2] R. C. Savage, "The radiative properties of hydrometeors at microwave frequencies," *J. Appl. Meteorol.*, vol. 17, pp. 904-911, 1978.
- [3] T. T. Wilheit, A. T. C. Chang, M. S. V. Rao, E. B. Rodgers, and J. S. Theon, "A satellite technique for quantitatively mapping rainfall rates over the oceans," *J. Appl. Meteorol.*, vol. 16, no. 5, pp. 551-560, 1977.
- [4] R. G. Isaacs, and G. Deblonde, "Millimeter wave moisture sounding: The effect of clouds," *Radio Sci.*, vol. 22, no. 3, pp. 367-377, 1987.
- [5] T. T. Wilheit, "An algorithm for retrieving water vapor profiles in clear and cloudy atmospheres from 183 GHz radiometric measurements: Simulation studies," *J. Appl. Meteorol.*, vol. 29, pp. 508-515, June 1990.
- [6] A. J. Gasiewski and D. H. Staelin, "Science requirements for passive microwave sensors on Earth science geostationary platforms," *Proceedings of the NASA Technology Workshop for Earth Science Geostationary Platforms*, NASA Conference Publication 3040, pp. 37-53, Sept. 21-22, 1988.
- [7] J. Simpson, R. F. Adler, and G. R. North, "A proposed Tropical Rainfall Measuring Mission (TRMM) satellite," *Bull. Amer. Meteor. Soc.*, vol. 69, pp. 278-295, 1988.

- [8] J. H. Van Vleck, "The absorption of microwaves by uncondensed water vapor," *Phys. Rev.*, vol. 71, pp. 425-433, 1947.
- [9] P. W. Rosenkranz, "Pressure broadening of rotational bands. II. Water vapor from 300 cm^{-1} to 1100 cm^{-1} ," *J. Chem. Phys.*, vol. 87, no. 1, pp. 163-170, July, 1987.
- [10] H. J. Liebe, "The atmospheric water vapor continuum below 300 GHz," *Int. J. Infrar. Millimeter Waves*, vol. 5, no. 2, pp. 207-227, 1984.
- [11] H. J. Liebe, "An updated model for millimeter wave propagation in moist air," *Radio Sci.*, vol. 20, no. 5, pp. 1069-1089, 1985.
- [12] H. J. Liebe, "A contribution to modeling atmospheric millimeter-wave properties," *Frequenz*, 41, vol. 41, pp. 31-36, 1987.
- [13] A. J. Gasiewski, "Atmospheric propagation loss measurements in the spectral window near 337 GHz," M. S. dissertation, Department of Electrical Engineering, Case Western Reserve University, Cleveland, OH, Aug. 1983.
- [14] J. M. Galm, F. L. Merat, and P. C. Claspy, "Estimates of atmospheric attenuation sensitivity with respect to absolute humidity at 337 GHz," *IEEE Trans. Antennas Propagat.*, vol. 38, pp. 982-986, July 1990.
- [15] P. W. Rosenkranz, "Interference coefficients for overlapping oxygen lines in air," *J. Quant. Spectrosc. Radiat. Transfer*, vol. 39, no. 4, pp. 287-297, 1988.
- [16] U. S. Standard Atmosphere, U. S. Government Printing Office, Washington, DC, 1976.
- [17] I. R. Dagg, G. E. Reesor, and M. Wong, "A microwave cavity measurement of collision-induced absorption in N_2 and CO_2 at 4.6 cm^{-1} ," *Can. J. Phys.*, vol. 56, pp. 1037-1045, 1978.
- [18] C. C. Kuo, "Statistical iterative scheme for estimating atmospheric relative humidity profiles from microwave radiometric measurements," S. M. thesis, Department of Electrical Engineering and Computer Science, Massachusetts Institute of Technology, Cambridge, MA, Dec. 1988.
- [19] C. C. Kuo and D. H. Staelin, "Statistical iterative scheme for estimating atmospheric relative humidity profiles," submitted for publication in *IEEE Trans. Geosci. Remote Sensing*, Sept. 1990.
- [20] D. Deirmendjian, "Far-infrared and submillimeter wave attenuation by clouds and rain," *J. Appl. Meteorol.*, vol. 14, pp. 1584-1593, 1975.
- [21] A. J. Gasiewski, "Microwave radiative transfer in hydrometeors," in *Atmospheric Remote Sensing by Microwave Radiometry*, M. A. Janssen, Ed. New York: John Wiley and Sons, in press, 1992, ch. 3.
- [22] J. S. Marshall and W. McK. Palmer, "The distribution of raindrops with size," *J. Meteor.*, vol. 5, pp. 165-166, 1948.
- [23] R. S. Sekhon and R. C. Srivastava, "Snow size spectra and radar reflectivity," *J. Atmos. Sci.*, vol. 27, pp. 299-307, 1970.
- [24] J. W. Waters, K. F. Kunzi, R. L. Pettyjohn, R. K. L. Poon, and D. H. Staelin, "Remote sensing of atmospheric temperature profiles with the Nimbus 5 Microwave Spectrometer," *J. Atmos. Sci.*, vol. 32, no. 10, pp. 1953-1969, 1975.
- [25] M. J. McFarland, R. L. Miller, and C. M. U. Neale, "Land surface temperature derived from the SSM/I passive microwave brightness temperatures," *IEEE Trans. Geosci. Remote Sensing*, vol. 28, pp. 839-845, Sept. 1990.
- [26] M. Yeh, Personal communication.
- [27] R. F. Adler, R. A. Mack, N. Prasad, H.-Y. M. Yeh, and I. M. Hakkarinen, "Aircraft microwave observations and simulations of deep convection from 18-183 GHz. Part I: Observations," *J. Ocean. Atm. Tech.*, vol. 7, pp. 377-391, June 1990.
- [28] A. J. Gasiewski, "Numerical sensitivity analysis of passive EHF and SMMW channels to tropospheric water vapor and precipitation," *Proceedings of the 1990 International Geoscience and Remote Sensing Symposium*, May 20-24, University of Maryland, College Park, MD, pp. 855-858, 1990.
- [29] C. Kummerow, R. A. Mack, and I. M. Hakkarinen, "A self-consistency approach to improve rainfall rate estimation from space," *J. Appl. Meteorol.*, vol. 28, no. 9, pp. 869-884, Sept. 1989.
- [30] A. Gagin, D. Rosenfeld, and R. E. Lopez, "The relationship between height and precipitation characteristics of summertime convective cells in South Florida," *J. Atmos. Sci.*, vol. 42, no. 1, pp. 84-94, Jan. 1985.
- [31] B. Kedem, L. S. Chiu, and Z. Karni, "An analysis of the threshold method for measuring area-average rainfall," *J. Appl. Meteorol.*, vol. 29, no. 1, pp. 3-20, Jan. 1990.
- [32] A. J. Gasiewski, J. W. Barrett, P. G. Bonanni, and D. H. Staelin, "Aircraft-based radiometric imaging of tropospheric temperature profiles and precipitation using the 118.75-GHz oxygen resonance," *J. Appl. Meteorol.*, vol. 29, no. 7, July 1990.
- [33] P. E. Racette, L. R. Dod, J. C. Shiue, R. F. Adler, D. M. Jackson, A. J. Gasiewski, and D. S. Zacharias, "Millimeter-wave imaging radiometer for cloud, precipitation, and atmospheric water vapor studies," *Proceedings of the IGARSS'92*, pp. 1426-1428, Houston, TX, May 26-29, 1992.



A. J. Gasiewski (SM'81-M'88) received the Ph.D. degree in electrical engineering and computer science from the Massachusetts Institute of Technology in 1988.

Since then, he has been a faculty member of the School of Electrical Engineering at the Georgia Institute of Technology. His interests include passive and active remote sensing (electromagnetic and acoustic), radiative transfer theory, continuum electrodynamics, communication and estimation theory, meteorology, statistical and quantum physics, and

electromagnetic and electronic instrumentation. His current research concerns the remote sensing of atmospheric water vapor and precipitation using satellite-based passive microwave sensors.

Dr. Gasiewski is the recipient of a Hewlett-Packard faculty development fellowship and a DuPont Young Faculty Grant, and received first place in the 1989 URSI student paper prize competition. He currently serves on the National Research Council's Committee on Radio Frequencies. He is a member of Eta Kappa Nu, Tau Beta Pi, IEEE, URSI (Commission F), Sigma Xi, and AGU.

Appendix B.

(Submitted for Presentation at the 1993 International Geoscience and Remote Sensing Symposium, Tokyo, Japan, August 18-23, 1993)

OPTIMAL CALIBRATION OF RADIOMETER USING WIENER FILTERS

L.K. Adelberg, A.J. Gasiewski and D.M. Jackson

School of Electrical Engineering

Georgia Institute of Technology, Atlanta, GA 30332, USA

PH: (404) 894-2934

FAX: (404) 853-9171

e-mail: agl4@prism.gatech.edu

In microwave radiometry, hot and cold blackbody targets of known temperature and emissivity are used to calibrate microwave radiometers. The calibration process involves estimating two slowly time-varying system parameters (the gain m and offset b) from noisy observations of these targets, where the output voltage $v = mT + B + n$, and n is an additive Gaussian white noise. Using only two observations, (v_{Hi} and v_{Ci}) along with known associated antenna temperatures (T_{Hi} and T_{Ci}), the pairwise estimates are:

$$m_i = \frac{v_{Hi} - v_{Ci}}{T_{Hi} - T_{Ci}} \quad b_i = \frac{v_{Ci}T_{Hi} - v_{Hi}T_{Ci}}{T_{Hi} - T_{Ci}}$$

Much of the error in the above estimates can be removed applying a non-causal, discrete linear filter:

$$\hat{m}_i = \sum_k w_k^m m_{i-k} \quad \hat{b}_i = \sum_k w_k^b b_{i-k}$$

The purpose of this paper is to discuss the application of optimal filters to radiometer calibration.

For observation sequences that are long compared to the gain and offset correlation times, an optimal linear filter (Wiener filter) can be used to minimize the mean-square errors $\hat{m}_i - m$ and $\hat{b}_i - b$ between the actual and estimated system parameters. Upon substitution for \hat{m}_i and \hat{b}_i , the errors become $\sum_k w_k^m m_{i-k} - m$ and $\sum_k w_k^b b_{i-k} - b$ which are squared and differentiated with respect to the filter coefficients w_k^m and set equal to zero. This will minimize the error with respect to the filter coefficients and produce the optimal filter.

In order to implement the filter, the autocorrelation functions R_k^m and R_k^b of the processes m , b and the noise standard deviation σ_n are estimated from the pairwise observations m_i and n_i . The Wiener filter coefficients are obtained from these statistical measurements. However, the underlying gain and offset parameters are not stationary and exhibit random jumps. In order to properly apply the Wiener filter, a method for detecting deviations in the statistical behavior of the pairwise estimates has been developed using the Z-test. If the ratio of the short time standard deviations exceeds a given threshold, a jump is detected. If so, the Wiener filter is shortened accordingly, and the filter coefficients renormalized.

The application of the above algorithm to data from the Millimeter-wave Imaging Radiometer (MIR) will be discussed. The MIR is a cross-track scanning radiometer with channels at 90, 150, $183 \pm 1, 3, 7$ and $325 \pm 1, 3, 7$ GHz. Recent data from flights of the MIR on the NASA ER-2 high-altitude aircraft during the Tropical Ocean Global Atmosphere (TOGA) Coupled Ocean/Atmosphere Response Experiment (COARE) will be presented.

(Proceedings of the 1992 IEEE Joint Symposia APS/URSI/EMP Meeting, pp. 412-415, presented in Chicago, IL, July 18-25, 1992.)

Electromagnetic Scattering from Microwave Absorbers: Laboratory Verification of the Coupled Wave Theory

A.J. Gasiewski, D.M. Jackson*
School of Electrical Engineering
Georgia Institute of Technology
Atlanta, GA 30332-0250

Laboratory W-band measurements of the bistatic scattering function of some common microwave absorbing structures have been made. The structures investigated include periodic wedge-type and pyramid-type iron-epoxy calibration loads and flat carbon-foam "Echosorb" samples (Table 1). Measurements were made using an HP 8510 network analyzer interfaced to a focussed-lens scattering range (Figure 1). The test set provided a dynamic range of ~ 55 dB. Swept frequency measurements over the band 75-100 GHz have revealed specular and Bragg reflection characteristics in the measured data.

The range consists of two mechanical booms (one each for the receiver and transmitter) that rotate about a common axis. A standard-gain horn and rexolite lens (focal length = 8.5 cm) are mounted on each boom and are aligned to produce a 4-cm (approximately) focussed spot on the sample under test, located on the axis of rotation. Both co- and cross-polarized reflection measurements for both TE- and TM-incident polarizations can be made. Figure 2 (A1 plate) shows the 90-GHz angular response of the range for a fixed incident angle (60°) and variable scattering angle.

In interpreting the data, the angular response of the system to the specular scattering from a flat aluminum plate is deconvolved from the measured reflectivities. Three deconvolution procedures are considered: Fourier transformation, linear minimum mean-square error estimation (LMMSE), and the CLEAN algorithm [1]. A major drawback of Fourier transformation is an enhancement of noise energy near the zeroes of the transformed angular response. The LMMSE technique is an implementation of a discrete non-causal Wiener filter and is less sensitive to measurement noise. The CLEAN algorithm was originally developed for radioastronomical image enhancement in which the measured data consisted of a two-dimensional distribution of point sources convolved with the response function of the radiotelescope. Since the bistatic scattering function of a periodic surface is an angular distribution of impulses, CLEAN is also well-suited for deconvolution of the W-band scattering measurements.

Theoretical calculations of the bistatic scattering coefficient for the

periodic wedge samples were performed using the coupled wave method [2, 3]. In this method, the periodic region between the peaks and troughs of the wedge structure is discretized into inhomogeneous horizontal layers. The permeability and permittivity in the layers are each represented as Fourier series. The EM fields within each layer are expressed as a sum of inhomogeneous plane waves. The fields above and below the wedge region are expressed as a sum of propagating and evanescent Floquet harmonics. By using Maxwell's curl equations, a set of coupled equations involving the unknown wave amplitudes is obtained. A solution for the amplitudes is found using eigenanalysis and EM-field boundary conditions at the interfaces to each layer. The numerical accuracy for the fields in each region is checked using conservation of energy.

Figure 2 is a comparison between calculated and measured co-polarized TM reflection at 90-GHz for sample #4 (wedge absorber), assuming $\epsilon_r = 9.0 - j0.4$ and $\mu_r = 1.0 - j0.5$. The computed location of the first Bragg lobe (-10.1°) is consistent with the measured response near this angle. Moreover, the calculated magnitudes of both the specular lobe and first Bragg lobe are consistent with the measured values. For this case, all other reflected harmonics are evanescent. The measured reflectivity for sample #5 showed evidence of several propagating harmonics, as predicted. For example, at 90 GHz and incident angle of 60° , there are 7 Bragg lobes. The laboratory measurements for the wedge absorbers also showed higher specular and Bragg reflection for TE-incident waves than for TM-incident waves, as expected.

Additional measurements were made for several other structures. Measured TM reflectivities for sample #2 (flat dielectric) showed only a small Brewster-angle null (~ 3 dB), indicating a complex permeability. Sample #3 (flat open-cell absorber sheet) exhibited a TE co-polarized specular reflectivity of ~ -10 dB at 90-GHz for 45° incidence. Due to the large electrical size of the cells, diffuse scattering was expected, but not observed in the raw data. For sample #6 (pyramid load), the dynamic range was insufficient to characterize the reflectivity. This was not unexpected since two-dimensionally periodic structures generally scatter energy over the entire upper hemisphere.

Acknowledgements: The authors wish to thank M. Bliesener and P. Doshi, E.E. School, Georgia Tech, and P. Friedrich, Georgia Tech Research Institute for their assistance in the measurements. The pyramidal absorber was provided by the ZAX Millimeter Wave Corporation.

This work was supported by NASA grant NAG 5-1490.

Sample #	Description
1	Flat Al plate
2	Flat Fe-epoxy slab
3	Flat carbon-foam "Echosorb" sheet (pore size ~ 0.5 mm)
4	Periodic wedge Fe-epoxy absorber (pitch=3.2 mm, depth=6.5 mm)
5	Periodic wedge Fe-epoxy absorber (pitch=12.5 mm, depth=24.0 mm)
6	Periodic pyramid Fe-epoxy absorber (pitch=10 mm, depth=40 mm)

Table 1: Description of samples used in the laboratory bistatic reflection measurements.

References

- [1] Thompson, A.R., J.M. Moran and G.W. Swenson, Interferometry and Synthesis in Radio Astronomy, Krieger Publishing Company: Malabar, Florida, 1991.
- [2] Gasiewski, A.J, D.M. Jackson, and A.F. Peterson, "Electromagnetic Scattering from Lossy Corrugated Surfaces: Application to Microwave Absorbers", *Proceedings of the 1991 URSI Radio Science Meeting*, p. 304, presented at the University of Western Ontario, London, Ontario, Canada, June 24-28, 1991.
- [3] Moharam, M.G., and T.K. Gaylord, "Diffraction Analysis of Dielectric Surface-Relief Gratings", *J. Opt. Soc. Am.*, 72, pp. 1385-1392, 1982.

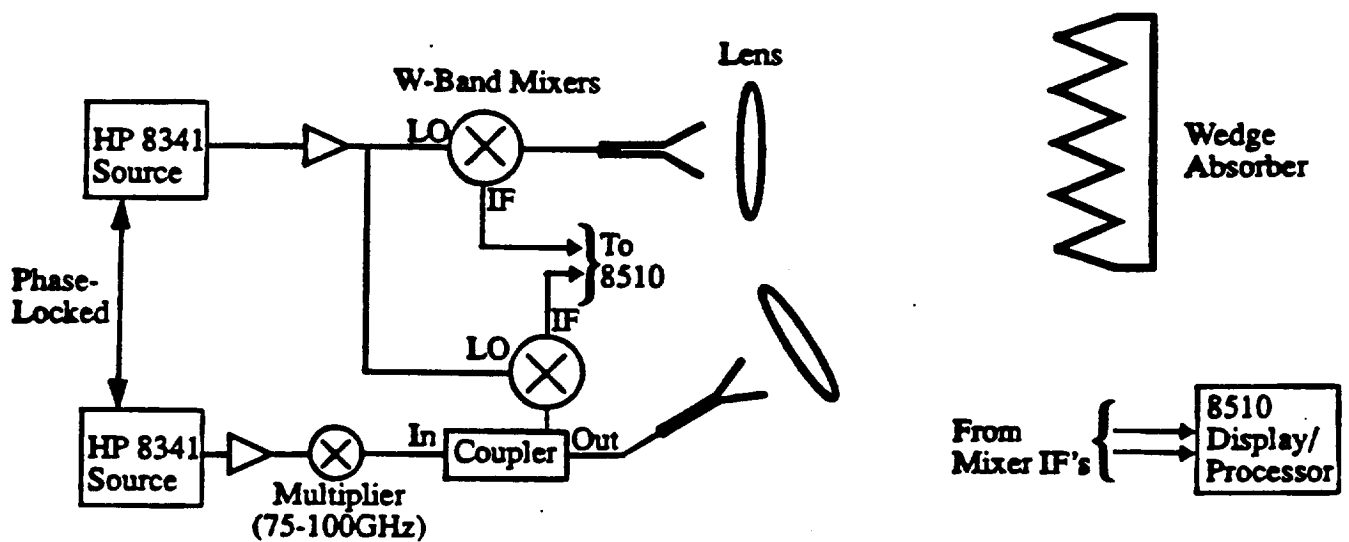


Figure 1: Schematic diagram of the focussed scattering range.

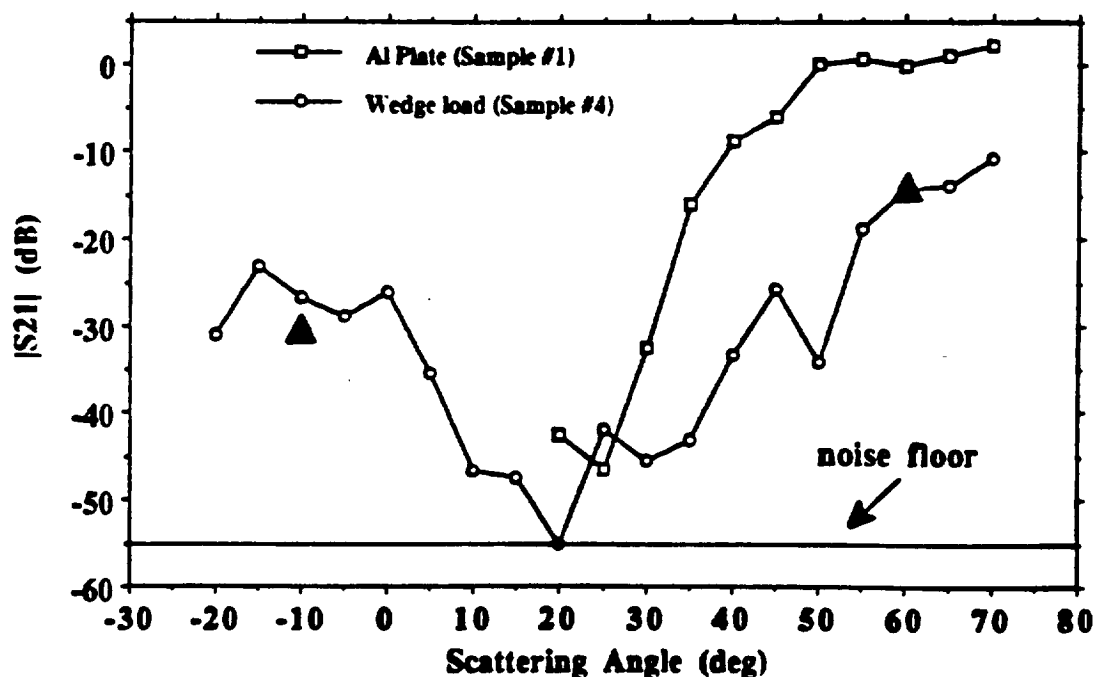


Figure 2: Measured reflectivity at 90 GHz and $\theta_i = 60^\circ$ for Sample #1 (Al plate) and #4 (wedge load) for TM-incident polarization. The grating vector is in the plane of incidence. The coupled-wave calculations for the specular and first Bragg directions (scattering angles 60° and -10.1° , respectively) are shown (\blacktriangle) for comparison.

Appendix D.

(Proceedings of the 1993 URSI National Radio Science Meeting, p 155, presented at the University of Colorado, Boulder, CO, Jan 5-8, 1993.)

Laboratory Measurements of Water Gravity Wave Characteristics Using Full Polarization Microwave Radiometry

D.B. Kunkee, A.J. Gasiewski
School of Electrical Engineering
Georgia Institute of Technology
Atlanta GA, 30332-0250

To demonstrate the usefulness of the full Stokes vector (T_v , T_h , $T_U = 2\text{Re}(E_v E_h^*)$ and $T_V = 2\text{Im}(E_v E_h^*)$) in determining the characteristics (i.e. direction) of ocean waves from satellite-based passive observations, radiometric emissions from a striated water surface under clear air background conditions were observed at 92 GHz. A Dicke-switched dual-polarized radiometer with additional circuitry to provide estimates of the four Stokes parameters (A.J. Gasiewski and D.B. Kunkee, "Calibration and Applications of Polarization Correlating Radiometers", accepted for publication in *IEEE Trans. Microwave Theory Tech* July, 1992) was used to obtain calibrated full polarimetric measurements over the entire range of water wave azimuthal angles ϕ_s . The measurements were compared to theoretical calculations based on the Kirchhoff approximation (KA) for a sinusoidal surface. The KA models the surface as a distribution of specularly reflecting facets, each of which contributes to the total observed radiation in accordance with the Fresnel reflectivity relations.

For sinusoidal water waves of $h/\Lambda = 0.05$ (where h is the peak amplitude and Λ is the water wavelength), the measured T_U amplitude is approximately $\pm 10^\circ K$ over $0^\circ \leq \phi_s \leq 360^\circ$ at an observation angle of $\theta_s = 65^\circ$ (see figure). The peak-to-peak variation of T_U is comparable to the measured variations of T_v and T_h . For near-nadir observations the T_U response decreases, but could be significant for some remote sensing applications. The wave tank measurements suggest that ocean wave direction will be observable (modulo 180°) using T_v , T_h , and T_U .

